

# Imaging bioluminescence by detecting localized haemodynamic contrast from photosensitized vasculature

Received: 22 May 2023

Accepted: 30 March 2024

Published online: 10 May 2024

 Check for updates

Robert Ohlendorf<sup>1,4,6</sup>, Nan Li<sup>1,5,6</sup>, Valerie Doan Phi Van<sup>1</sup>, Miriam Schwalm<sup>1</sup>, Yuting Ke<sup>1</sup>, Miranda Dawson<sup>1</sup>, Ying Jiang<sup>1</sup>, Sayani Das<sup>1</sup>, Brenna Stallings<sup>1</sup>, Wen Ting Zheng<sup>1</sup> & Alan Jasanoff<sup>1,2,3</sup>✉

Bioluminescent probes are widely used to monitor biomedically relevant processes and cellular targets in living animals. However, the absorption and scattering of visible light by tissue drastically limit the depth and resolution of the detection of luminescence. Here we show that bioluminescent sources can be detected with magnetic resonance imaging by leveraging the light-mediated activation of vascular cells expressing a photosensitive bacterial enzyme that causes the conversion of bioluminescent emission into local changes in haemodynamic contrast. In the brains of rats with photosensitized vasculature, we used magnetic resonance imaging to volumetrically map bioluminescent xenografts and cell populations virally transduced to express luciferase. Detecting bioluminescence-induced haemodynamic signals from photosensitized vasculature will extend the applications of bioluminescent probes.

Bioluminescent reporters are widely applied in basic and preclinical biology<sup>1,2</sup>. These proteins generate light by converting substrates into excited-state products that electronically relax by photon emission. By rendering luminescent enzyme activity contingent on genetic or biochemical events, a broad range of molecular and cellular processes can be studied using optical detection. Bioluminescence imaging (BLI) permits spatially resolved monitoring of luminescent reporters with high sensitivity, due to the complete absence of endogenous light sources in most organisms<sup>3,4</sup>. Localization of bioluminescent probes in vivo is nevertheless severely compromised by scattering and attenuation of emitted light in bone and soft tissue. This is particularly a problem in the brain, where the skull impedes photon propagation, especially at short wavelengths<sup>5</sup>. As a result, BLI data are often limited in resolution and heavily biased toward superficial sources, and most BLI images are obtained in the form of two-dimensional projections that lack depth information. Bioluminescence tomography<sup>6,7</sup> addresses

this problem by using diffuse optical reconstruction methods to estimate three-dimensional light source positions in scattering tissue, but this approach usually requires a priori knowledge about the source distribution as well as registration with anatomical information from an independent imaging modality.

Another way to circumvent limitations of conventional BLI would be to devise a method for converting bioluminescent output locally into a different type of signal that could be imaged in deep tissue using established non-invasive modalities such as X-ray tomography, ultrasound or magnetic resonance imaging (MRI). Although probe architectures for reversibly transducing light into MRI-detectable signals in particular have been introduced<sup>8–13</sup>, imaging approaches using them so far lack the resolution or sensitivity to support in vivo BLI applications. We recently showed that engineered proteins and peptides could be used to convert molecular signals into changes in blood flow that can be sensitively detected using MRI or other haemodynamic imaging

<sup>1</sup>Department of Biological Engineering, Massachusetts Institute of Technology, Cambridge, MA, USA. <sup>2</sup>Department of Brain and Cognitive Sciences, Massachusetts Institute of Technology, Cambridge, MA, USA. <sup>3</sup>Department of Nuclear Science and Engineering, Massachusetts Institute of Technology, Cambridge, MA, USA. <sup>4</sup>Present address: Max Planck Institute for Biological Cybernetics, Tübingen, Germany. <sup>5</sup>Present address: Advanced Imaging Research Center and Department of Neuroscience, University of Texas Southwestern Medical Center, Dallas, TX, USA. <sup>6</sup>These authors contributed equally: Robert Ohlendorf, Nan Li. ✉e-mail: [jasanoff@mit.edu](mailto:jasanoff@mit.edu)

techniques. These haemodynamic imaging agents have been applied as exogenous vasoactive probes for small molecules<sup>14</sup> and enzymes<sup>15,16</sup> or endogenously expressed 'haemogenetic' reporters for intracellular calcium signalling<sup>17</sup>. In each case, the probes leverage the biological amplification afforded by vasodilation reflexes, the dense spatial sampling afforded by the vascular network (all tissue less than 30  $\mu\text{m}$  from vessels in rodent brain)<sup>18</sup>, and the sensitivity with which vascular responses can be imaged. We reasoned that a related approach might be effective at converting photon emission from bioluminescent reporters into haemodynamic signals, thus providing a means for performing spatially resolved BLI in deep tissue and an alternative to constructing specialized reporters for non-invasive imaging modalities<sup>19</sup>.

In this study, we implement the strategy of BLI using haemodynamics (BLUsH). We demonstrate that expression of a light-activated protein in vascular cells enables these cells to sense photon output from bioluminescent reporters and, thereupon, generate haemodynamic signals detectable in effective longitudinal relaxation time ( $T_2^*$ )-weighted MRI. We apply BLUsH to detect bioluminescent cell implants and track viral expression of bioluminescent transgenes in deep brain areas of living rats. BLUsH thus provides a basis for connecting powerful optical reporter technology to state-of-the-art haemodynamic imaging in deep tissue. We anticipate that this synthesis will enable a diversity of molecular and cellular process to be studied over a range of spatiotemporal scales in living animals of any size.

## Results

### Characterization of BLUsH components in vitro

In the BLUsH paradigm, bioluminescent reporters activate light-dependent photoreceptor proteins expressed in vascular cells and stimulate downstream signalling cascades. These signalling events, in turn, cause local dilation of blood vessels and haemodynamic contrast detectable by MRI or other imaging modalities (Fig. 1a). Haemodynamic changes can result from a variety of signalling pathways that ultimately inhibit or activate contraction of vascular smooth muscle cells (VSMCs)<sup>20–22</sup>, leading to dilation or constriction of blood vessels and affecting blood flow, volume and oxygenation. We previously engineered imaging probes that promote vasodilation via G-protein-coupled receptor-mediated cyclic adenosine monophosphate (cAMP) signalling in response to target molecular cues, such as enzymatic activity or signalling molecules<sup>14–16</sup>. For our initial implementation of BLUsH, we therefore decided to use the photoactivated adenylate cyclase from the bacterium *Beggiatoa* (bPAC)<sup>23</sup> to intervene similarly, by producing intracellular cAMP in VSMCs in response to blue illumination.

To assess the feasibility of BLUsH imaging, we first characterized the light production of relevant bioluminescent enzymes. The luciferases that catalyse blue light production from coelenterazine (CTZ) substrates have been widely applied as reporters and sensors<sup>1,2</sup>, including for stimulation of optogenetic actuators<sup>24</sup>. CTZ-dependent enzymes are known for their brightness, and the attenuation of their short wavelength emission in tissue is likely to promote the near-field detection specificity we seek to obtain in the BLUsH approach. We compared the luminescence outputs of three blue luciferases, NanoLuc<sup>25</sup> and engineered Gaussia luciferase (GLuc) variants sbGLuc and GLucM23 (ref. 26). The outputs of all luciferases are on the same order of magnitude (Fig. 1b), but GLucM23 is 30–300% brighter than the other two; we therefore resolved to work with this protein. To get a realistic estimate of achievable light levels in vivo, we characterized the bioluminescence of GLucM23-expressing cells at quantities and substrate doses suitable for application in animals (250,000 cells, 95  $\mu\text{M}$  CTZ). After a peak intensity of  $9.9 \pm 1.6 \mu\text{W cm}^{-2}$  the bioluminescence output (Fig. 1c,d) decays with a half life of 3.7 min (95% confidence interval 3.6–3.8 min) (Fig. 1e). These parameters define timing and sensitivity requirements for BLUsH imaging of luciferase-expressing cells.

We next examined the ability of bPAC to activate signalling pathways in a light-dependent fashion in a Chinese hamster ovary (CHO) cell-based assay that quantitatively reports intracellular cAMP levels (Fig. 1f). Illumination with a blue light-emitting diode (LED,  $465 \pm 10 \text{ nm}$ ,  $\sim 300 \mu\text{W cm}^{-2}$ ) induced cAMP production in bPAC-expressing reporter cells, but no notable response in control cells (Fig. 1g,h). When examined over a range of LED powers, the relative bPAC light response saturated with a half maximal effective dose of  $26 \pm 9 \mu\text{W cm}^{-2}$  (Fig. 1i); this is about twice the bioluminescent cell output and is consistent with previous findings in bacterial fluorescence assays<sup>27</sup>. To test whether light output from bioluminescent cells is sufficient to induce equivalent responses, we exposed reporter cells expressing bPAC or control genes to luminescence from 250,000 GLucM23-expressing human embryonic kidney (HEK) cells incubated with 95  $\mu\text{M}$  CTZ. Only bPAC-expressing cells showed substantial light-induced cAMP production (Fig. 1j). We also demonstrated bPAC expression and blue light-sensitive activity using the bioassay of Fig. 1f implemented in cultured VSMCs (Fig. 1k). These results predict that bPAC should be able to promote haemodynamic responses at light doses achieved by bioluminescent reporters expressed intracellularly under biologically relevant conditions.

### In vivo imaging of photosensitized vasculature

Our implementation of BLUsH depends on converting endogenous blood vessels into light detectors using bPAC. To achieve bPAC expression in the cerebral vasculature of wild type rats, we used a dual adeno-associated virus (AAV) system (Fig. 2a). The first AAV encodes green fluorescent protein (GFP)-fused Cre recombinase under control of the SM22 $\alpha$  promoter, which directs smooth muscle-specific expression<sup>28,29</sup>. The second AAV encodes loxP-flanked bPAC, equipped with epitope and fluorescent protein tags and placed under control of a strong constitutive promoter. Before attempting in vivo studies, we determined that infection with both viruses leads to bPAC expression in cultured VSMCs (Supplementary Fig. 1). Correspondingly, co-injection into cortical or striatal brain regions in rats results in strong bPAC expression in vascular structures (Fig. 2b,c and Extended Data Fig. 1). Limitations of this approach include uneven labelling of vessels as well as some apparent off-target expression, but more homogeneous and specific brain-wide expression of bPAC could be achieved following intraventricular injection of an engineered Cre-dependent bPAC viral vector<sup>30</sup> into SM22 $\alpha$ -Cre transgenic mice (Extended Data Fig. 2). No indication of vascular hyperactivity was seen following staining for the inflammatory marker nitrotyrosine (Extended Data Fig. 3). Staining for the microglial marker Iba1 likewise revealed little evidence of inflammation-associated microglial activation in bPAC-treated brain tissue (Extended Data Fig. 4).

To assess the ability of bPAC-expressing vessels to function as light detectors in imaging experiments, we began by examining responses to exogenous illumination in brain regions transduced with virus mixtures. The MRI measurements were acquired using echo planar imaging (EPI) with parameters suitable for effective detection of haemodynamic signals in rodents at high magnetic field strengths<sup>31,32</sup>. Consistent with previous optogenetic studies<sup>33</sup>, illumination with blue LED emission delivered through a fibre-elicited robust signal changes in light-sensitized brain areas but not in areas exposed to illumination in the absence of viral pre-treatment (Fig. 2d and Extended Data Fig. 5). The time courses of the signal in regions of interest (ROIs), defined with respect to fibre positions, reveal that light responses begin seconds after the LED is switched on and then decay to baseline in minutes (Fig. 2e). The peak signals during illumination averaged  $5.1 \pm 0.8\%$  in responsive and  $-0.1 \pm 0.2\%$  in non-responsive brains, a significant difference with Student's *t*-test  $P = 0.014$  ( $n = 4$ ) (Fig. 2f).

The spatial distribution of MRI responses to illumination corresponds approximately to bPAC expression profiles visualized by immunohistochemistry (Fig. 2g and Supplementary Fig. 2). The response

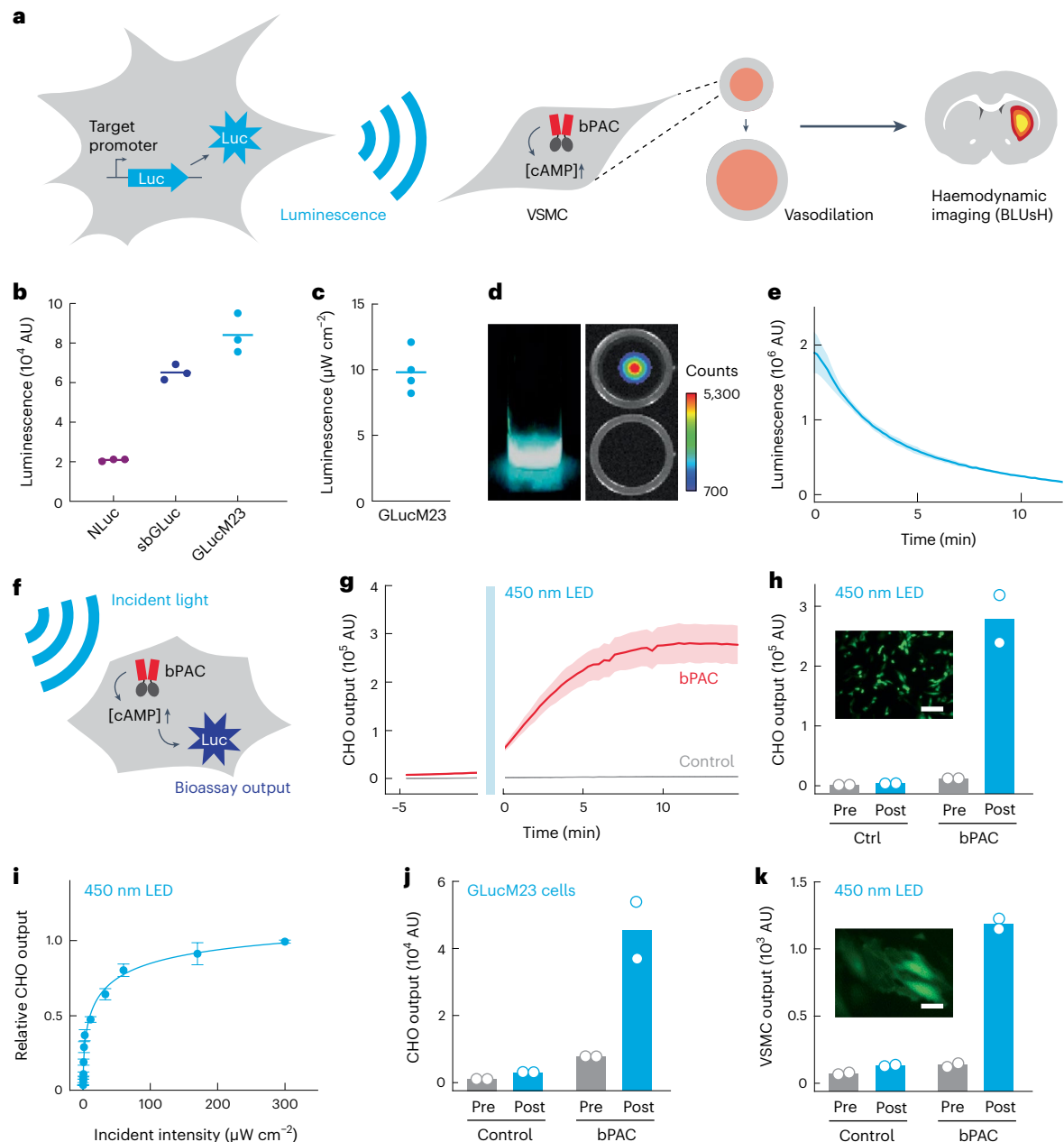


**Fig. 1 | Characterization of BLUsH components.** **a**, In the BLUsH mechanism, VSMCs are photosensitized by expression of the light-activated adenylate cyclase bPAC. Light emission by cells expressing luciferase reporters (blue) triggers bPAC-mediated vasodilation and subsequent haemodynamic imaging signals. **b**, Comparison of luminescence output of three luciferases. **c**, Quantification of peak light output by GLucM23-expressing HEK cells (~250,000 cells per measurement). **d**, Visualization of luminescent cells (left) and measurement in a standard BLI system (right). **e**, The time course of bioluminescence signal from HEK cells expressing GLucM23, following addition of a single dose of CTZ; the shading denotes the standard deviation of three biological replicates. **f**, Schematic of a bioassay for measuring blue light-dependent bPAC activation via activation of a cAMP-sensitive luminescent reporter. **g**, CHO cell-based bioassay results

comparing LED stimulation of bPAC-expressing (red) versus the control cells (grey). The shading denotes the standard deviation of three biological replicates. **h**, Amplitudes of signal observed in the CHO bioassay before (grey) and after (blue) LED stimulation. The inset denotes the CHO bioassay cells (green) with the scale bar, 100  $\mu\text{m}$ . **i**, Relative CHO bioassay output as a function of LED stimulation intensity. The data points denote the mean values and the error bars denote the standard deviations of three biological replicates, all normalized to responses at 300  $\mu\text{W cm}^{-2}$  illumination. **j**, The CHO bioassay output before (grey) and after (blue) stimulation by exposure to GLucM23-expressing HEK cells (250,000 cells at -15 mm distance). **k**, The reporter output from VSMCs expressing bioassay components before (grey) and after (blue) LED stimulation as in **g** and **h**. The inset denotes VSMC bioassay cells (green) with the scale bar, 100  $\mu\text{m}$ .

amplitudes fall off with distance from the fibre tip (Fig. 2h), with a depth dependence similar to light quantification results recently reported for blue illumination in brain tissue. Neither the response rise rate ( $k_{\text{on}}$ ) nor the decay rate ( $k_{\text{off}}$ ) vary substantially with distance from the fibre tip, however (Fig. 2i), indicating that response dynamics probably depend more on physiological response time courses than on photon absorption kinetics. Both haemodynamic signal change peaks and integrated response amplitudes vary monotonically with illumination

intensity (Fig. 2j), suggesting a broad, albeit nonlinear, dynamic range for vascular light sensing. Importantly, strong responses are observed with light doses as low as 0.1 mW  $\text{cm}^{-2}$ , comparable to levels reported in Fig. 1, suggesting relevance of the in vitro results to performance of the BLUsH mechanism in vivo. These results thus demonstrate that vascular bPAC expression can mediate haemodynamic responses suitable for mapping illumination profiles in the rodent brain, providing a basis for BLUsH imaging of endogenous luminescent probes.

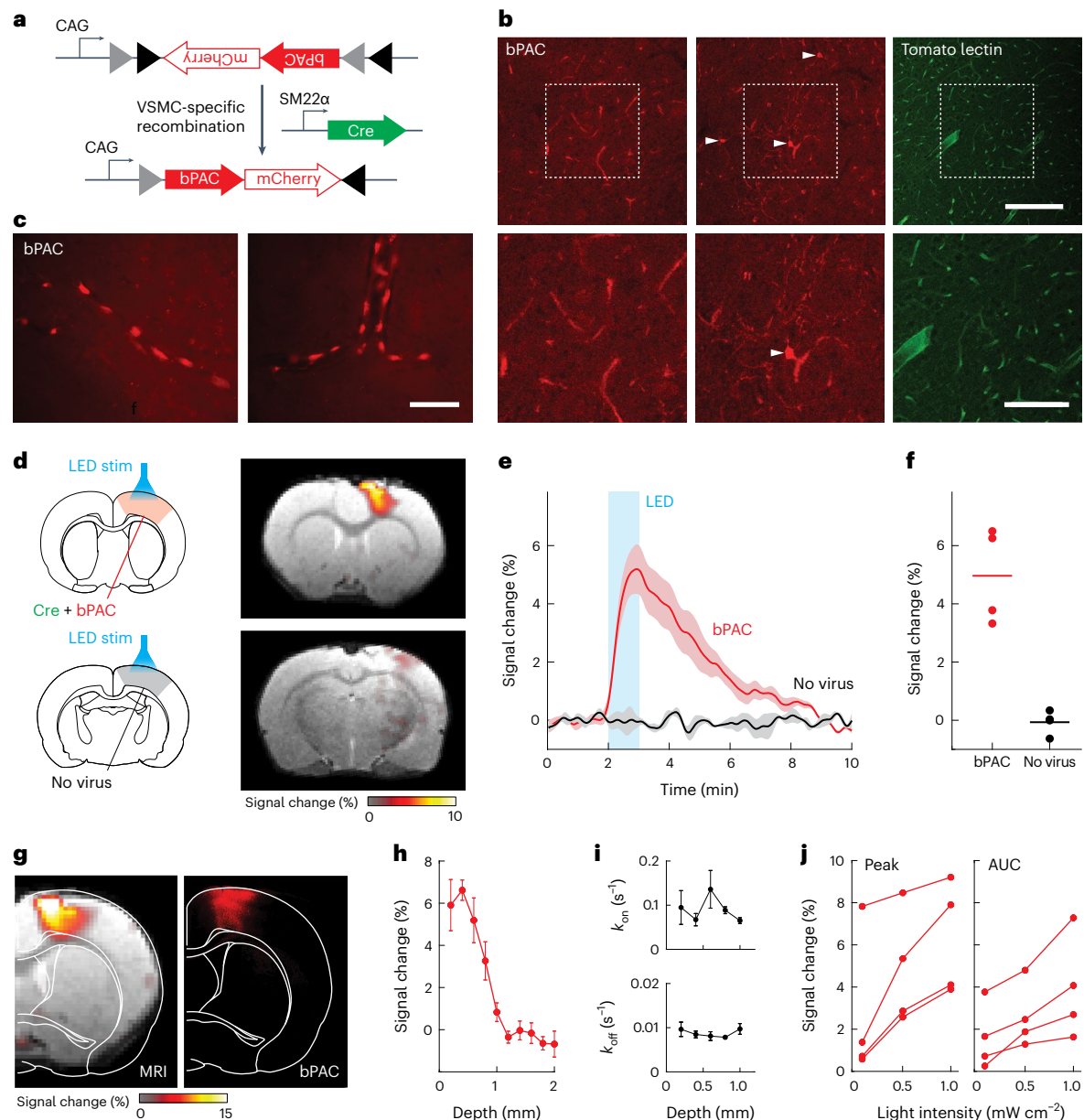


**Fig. 2 | Evaluation of photosensitized vasculature.** **a**, VSMC-restricted expression is achieved by delivering a Cre-activatable AAV encoding bPAC flanked by loxP sites (arrowheads, top) in combination with a second AAV encoding Cre under control of the VSMC-specific SM22 $\alpha$  promoter (right), resulting in constitutive expression of bPAC under control of a CAG promoter (bottom). **b**, Vascular expression profile confirmed by comparing bPAC expression patterns in two fields of view (red) with tomato lectin vascular staining in a different animal (green). The arrowheads indicate labelled structures with neuronal morphology, possibly reflecting off-target bPAC expression. Scale bars, 200  $\mu$ m (top) and 100  $\mu$ m (bottom). **c**, Images showing bPAC expression in individual cells spaced along large individual vessels. Scale bar, 100  $\mu$ m. **d**, Mean functional MRI responses to fibre-mediated light

stimulation schematized at left in BLUSH-treated (top) versus control (bottom) brain sites ( $n = 4$  each). **e**, Time courses of signal change in response to LED stimulation (blue rectangle) in BLUSH (red) and control (black) conditions. The shading denotes the s.e.m. of four measurements. **f**, Peak response amplitudes observed in the experiments of **d** and **e**. **g**, Correspondence of a BLUSH MRI response profile (left) with the bPAC expression visualized by histology (right). **h**, Responses to 1  $\text{mW cm}^{-2}$  stimulation as a function of depth from the fibre tip. The error bars are the s.e.m. of  $n = 4$ . **i**, On (top) and off (bottom) rates of BLUSH responses as a function of depth. The error bars are the s.e.m. of  $n = 4$ . **j**, BLUSH responses to varying light intensity in four experiments. The peak signal (left) and integrated area under the curve (AUC, right) are both shown.

### BLUSH imaging of luminescent xenografts

A common application of conventional BLI is the tracking of luminescent reporter-expressing cells *in vivo*, but accomplishing this in the brain is particularly challenging. To assess the ability of BLUSH to detect luciferase expression *in vivo*, we therefore examined whether the method could enable luminescent cell visualization in deep brain tissue. We established BLUSH detection regions in the striatum of healthy rats by injecting AAVs encoding vessel-targeted bPAC. The control regions expressing a fluorescent marker in place of bPAC were established in

contralateral hemispheres. After 6 weeks to permit BLUSH vascular light sensitivity to develop, xenografts of 500,000 cells expressing GLucM23 luciferase, equivalent to those used in the experiments of Fig. 1, were implanted into the photosensitized and control brain regions (Fig. 3a).

To perform BLUSH imaging of the xenografts, continuous MRI scanning was performed before, during and after CTZ substrate infusion via intracranial cannulas implanted over the bioluminescent cells. This procedure induced large haemodynamic signals in the area of the



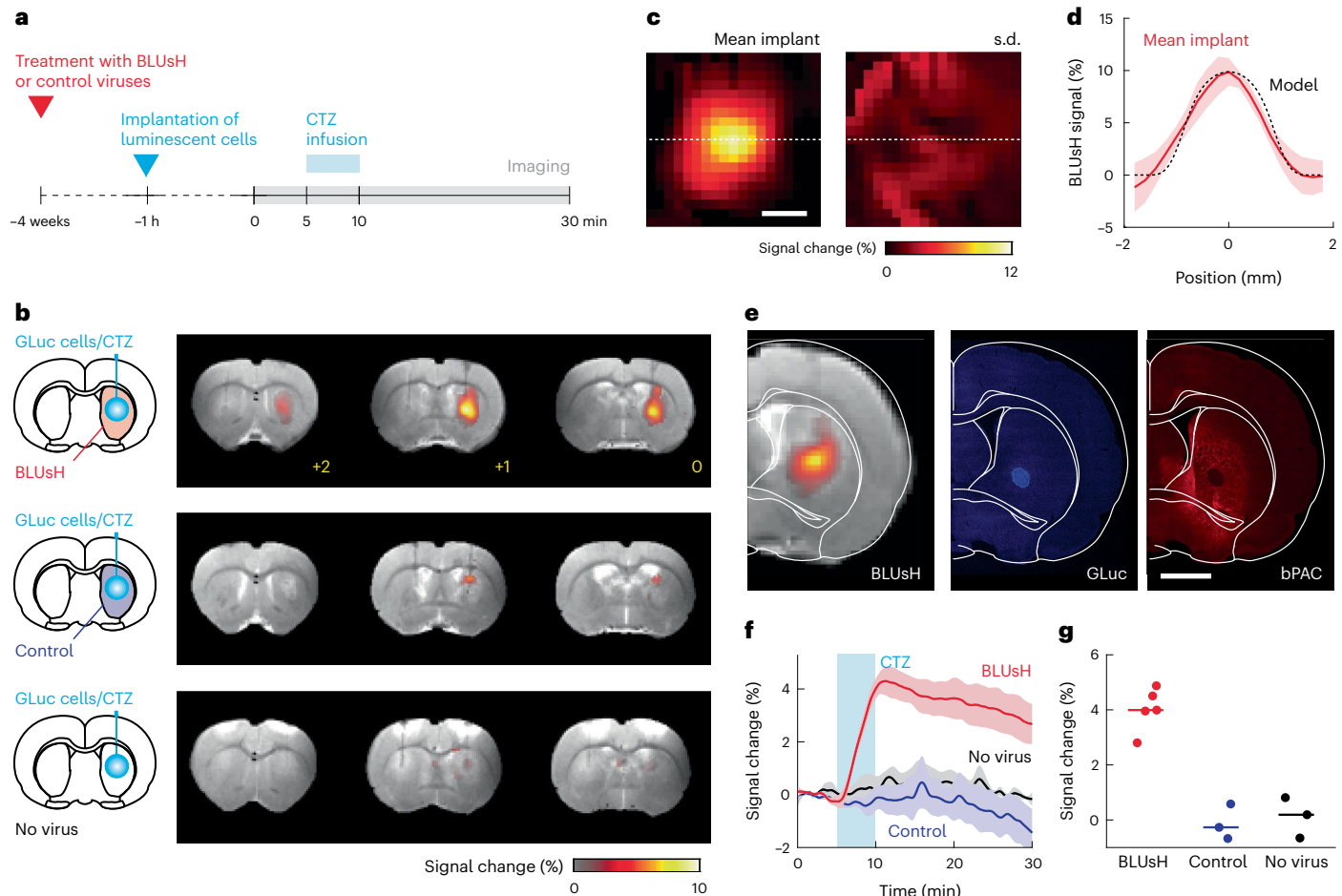


**Fig. 3 | Deep brain BLUsH imaging of luminescent xenografts.** **a**, Timeline of experiments showing viral infection time (red arrowhead), cell implantation (blue arrowhead), imaging (grey bar) and CTZ infusion period (blue rectangle). **b**, Average MRI results from xenograft imaging with BLUsH (top,  $n = 5$ ), in the presence of a control virus (middle,  $n = 3$ ) and in untreated brain tissue (bottom,  $n = 3$ ). Bregma coordinates in yellow. Schematics (left) diagram the experimental conditions. **c**, Closeup of mean signal from BLUsH xenograft imaging (left) with the standard deviation (s.d.) over five experiments shown on the same colour scale (right) to indicate consistency of the results. Scale bar, 1 mm. **d**, Comparison of mean BLUsH signal (red line, the shading is the s.d. of  $n = 5$ ) with a model profile

expected from a 1 mm implant (black dashed line). The BLUsH curve corresponds to a cross section through the image in **c** (white dashed line). **e**, Comparison of BLUsH and histology data from a representative animal. Scale bar, 2 mm. **f**, Signal time courses showing signal changes elicited by CTZ delivery (blue rectangle) in BLUsH imaging (red), control virus-treated tissue (purple) and untreated tissue (black). The shading is the s.e.m. of five (BLUsH) or three (control and no virus conditions) biological replicates. **g**, Peak signal changes observed following CTZ delivery in BLUsH and control experiments. The lines indicate average peak signal changes and the dots the values of single biological replicates for each group.

xenografts implanted in photosensitized brain hemispheres, but not in control non-bPAC virus-treated or untreated regions (Fig. 3b). The mean maps of the positive BLUsH responses averaged over experiments reveal a compact spatial profile with minimal standard deviation over animals (Fig. 3c), whereas control data from luminescent cells in untreated tissue remain within the error of baseline (Supplementary Fig. 3). BLUsH signal arising from the luminescent cells displays an average full width at half maximum (FWHM) of  $1.3 \pm 0.2$  mm ( $n = 5$ ), similar to the signal width predicted for an implant with 1 mm diameter (Fig. 3d). This is also consistent with visualization of representative implants by post-mortem histology (Fig. 3e), illustrating the approximate spatial correspondence of BLUsH signal changes with the location of luminescent cells in light-sensitized brain tissue. Conventional BLI with a high-sensitivity camera was also able to visualize equivalent luciferase-expressing cell implants in vivo (Extended Data Fig. 6) but with a FWHM of  $2.6 \pm 0.3$  mm that was more than twice the xenograft diameter and significantly greater than the BLUsH FWHM ( $t$ -test  $P = 0.01$ ,  $n = 4$  and 5). The xenografts expressing GLucM23 and the red-shifted luciferase Akaluc<sup>34</sup> (both  $n = 2$ ) displayed similar FWHM in this analysis.

The time course of BLUsH MRI responses in the cell implant experiments shows a rise within seconds of CTZ infusion that is not observed in control non-BLUsH conditions (Fig. 3f). Analysis of the effective dose of CTZ delivery versus signal change indicates a monotonic increase in the BLUsH response as a function of estimated tissue CTZ concentration, a result that approximately tracks measurements of luminescent output as a function of CTZ concentration in vitro (Supplementary Fig. 4). Furthermore, BLUsH signal increases with similar spatial profile can be elicited repeatedly by injecting CTZ over multiple distinct cycles, with the signal near the infusion site returning to baseline between injections (Extended Data Fig. 7). The mean peak amplitude for BLUsH signal following a single CTZ infusion was  $4.0 \pm 0.4\%$  (Fig. 3g), a significant response with Student's  $t$ -test ( $P = 0.006$ ,  $n = 5$ ). In contrast, control signal changes from luminescent cells in the absence of bPAC expression were negligible ( $t$ -test  $P \geq 0.73$ ,  $n = 3$ ). This indicates that responses to CTZ infusion could not be attributed to the infusion itself or to correlates of GLucM23 activity unrelated to light production, such as consumption of  $O_2$  or generation of  $CO_2$ . Although  $CO_2$  in particular can evoke haemodynamic signal increases under our imaging conditions (Supplementary Fig. 5), such responses are absent from our bPAC-free controls.

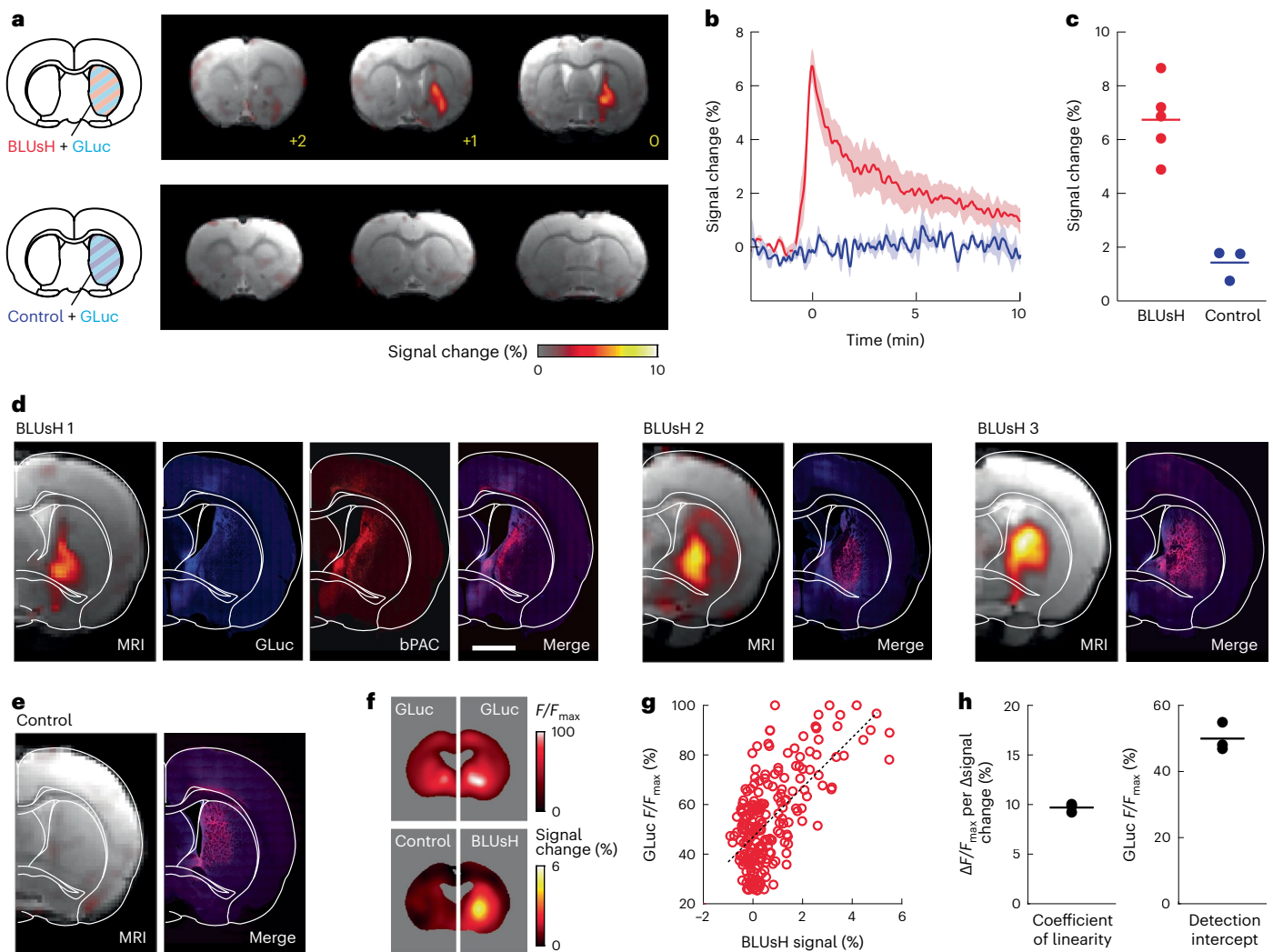


**Fig. 4 | BLUSH imaging of endogenous luciferase expression.** **a**, BLUSH (top) or control (bottom) imaging of brain regions from representative animals transduced with viruses as schematized and treated intravenously with CTZ to elicit responses. Bregma coordinates are denoted in yellow. **b**, Time courses of BLUSH (red) and control (purple) MRI signal aligned to peak response times (time, 0 min). The shading indicates the s.e.m. of five (BLUSH) or three (control) experiments. **c**, Peak signal changes observed in BLUSH and control experiments. The lines indicate average peak signal changes and the dots indicate values of single biological replicates for each group. **d**, Comparison of signal change profiles detected by MRI-based BLUSH versus post-mortem histology of GLucM23 and bPAC expression

in individual animals, showing correspondence of profiles at an individual animal level. Scale bar, 2 mm. **e**, Null signal changes observed in a control virus-treated animal (left) compared with the histology of GLucM23 and bPAC (right) in the same animal. **f**, Spatial alignment of co-registered GLucM23 histology (top) and MRI (bottom) images indicating overlap of signals in BLUSH (right) but not control (left) brain regions. **g**, Correspondence of GLucM23 histology and BLUSH signal changes in 226 voxels (dots) across three animals, revealing a strong correlation (dashed regression line; Pearson correlation  $r = 0.64$ ,  $P < 0.001$ ). **h**, Consistency of slope (left) and intercept (right) of the regression lines relating BLUSH signal to histological measures of GLucM23 expression in three animals.

### BLUSH imaging of optical reporter expression in the brain

Bioluminescent reporters expressed directly in brain cells can be used to monitor a variety of neural processes<sup>35</sup>. To assess whether BLUSH could enable such applications to be performed with spatial resolution in deep tissue, we tested that ability of BLUSH to visualize endogenous luciferase expression in virally transduced cells in situ. Light-sensitive and control brain regions were again established in individual animals using the dual AAV transduction approach of Figs. 2 and 3. To express the luciferase reporter, a third AAV encoding GLucM23 was co-administered with the BLUSH or control treatments.

BLUSH imaging was performed using MRI 6 weeks after viral injection. To achieve unbiased detection of luciferase activity throughout the brain, CTZ was administered systemically via the tail vein. The responses in the area of viral treatment were observed in BLUSH but not control animals (Fig. 4a and Extended Data Figs. 8 and 9). Peak signal changes were observed up to 25 min after CTZ injection and declined with an average half time of 4.1 min (95% confidence interval

3.2–5.5 min) (Fig. 4b). The mean amplitude of the peak signal change observed in BLUSH experiments was  $6.7 \pm 1.4\%$  (significant with  $t$ -test  $P = 0.0004$ ,  $n = 5$ ), whereas the average peak signal change in control regions was  $1.4 \pm 0.6\%$  ( $P = 0.05$ ,  $n = 3$ ) (Fig. 4c).

Notably, patterns of MRI signal change following intravenous CTZ delivery approximately corresponded to luminescent reporter expression patterns at the level of individual BLUSH animals but not controls (Fig. 4d,e and Extended Data Fig. 10), demonstrating the robustness of the visualization. To quantify this correspondence, we registered histological and MRI data into a common space and compared the results on a voxel level after smoothing. The correlation coefficient between BLUSH and immunohistochemical fluorescence levels was 0.64 across 226 voxels in three animals, which represents a significant correspondence with  $P < 10^{-4}$  (Fig. 4g). An approximately linear relationship between luciferase expression and BLUSH signal was consistent, with similar slopes and intercepts across animals (Fig. 4h). These results therefore demonstrate that BLUSH yields accurate, spatially resolved

measurements of endogenously expressed luminescent reporters in opaque brain tissue.

## Discussion

Surpassing current limitations of optical imaging is a major goal in biotechnology development, and strategies for mapping light in deep tissue are particularly sought after<sup>36</sup>. The BLUsH approach achieves this by converting cerebral vessels into photodetectors, in effect turning the tissue itself into a near-field biological camera. We applied BLUsH in the brain, where inter-vessel spacing is on the order of cellular dimensions, but in principle, BLUsH could be utilized in other areas as well. To detect BLUsH-based responses, we used MRI, which is known for its unlimited coverage and depth penetration, as well as sensitivity to a variety of vascular and complementary non-vascular contrast mechanisms. We show that MRI-based BLUsH imaging can be used to image luminescent implanted cells and virally induced endogenous luciferase expression in opaque, anatomically defined contexts, revealing three-dimensional distributions of luminescent-probe expression that are difficult to measure using stand-alone optical techniques in deep tissue.

The photon sensitivity of BLUsH arises from multiple enzymatic amplification factors, including the light-dependent actuator bPAC and downstream signal transduction components that directly drive VSMC relaxation and vasodilation. The dynamic range and linearity of BLUsH detection can be further characterized in specific applications. The data presented here suggest that a range of luminescent cell densities can be distinguished, but additional experiments could be applied to assess haemodynamic response properties in different tissue types or brain regions. Although vascular physiology could, in principle, be affected by O<sub>2</sub> consumption or CO<sub>2</sub> generation associated with luciferase activity, we did not observe evidence of this in any of our control measurements. This indicates that luciferase-catalysed gas perturbations are too subtle to cause substantial haemodynamic responses on their own, consistent with the fact that the CTZ stoichiometry of our experiments predicts peak gas changes far below basal rates reported in rat brain<sup>37</sup>. On the other hand, we cannot entirely rule out unpredicted pathways for BLUsH signal generation that still rely on bPAC activation. A drawback of our vessel-dependent optical imaging strategy is that it obeys slower kinetics than most electronic or chemical light detectors. Nevertheless, response times of the BLUsH mechanism were shown to be on the order of seconds, meaning that time-resolved measurements from luminescent reporters could be possible on this temporal scale.

Spatially, resolution of the BLUsH technique is enhanced when using blue-light emitters, such as GLucM23, because their short wavelength output is more restricted to sites of reporter activity in tissue. The requirement for close proximity between luminescent cells and photosensitized vessels thus serves to improve spatial resolution. We found that BLUsH resolved the dimensions of cell implants and the distribution of endogenous luciferase expression, suggesting that the resolution of BLUsH images is well under 1 mm and probably limited by the in-plane MRI voxel dimension of 400  $\mu$ m. The correlation between BLUsH and histology data in Fig. 4 was highly statistically significant but probably limited to some extent by resolution differences, misalignment between the MRI and histology slices, contributions from background fluorescence and the fact that underlying signal sources in MRI and histology are different. A more advanced assessment could be performed by comparing MRI-based visualizations with volumetric histology datasets, possibly obtained from cleared tissue<sup>38</sup>.

Equally important for future studies will be strategies for more uniform photosensitization of blood vessels than we have used for our initial BLUsH experiments here. This is particularly necessary for comprehensive mapping of luminescent reporters, given the requirement for spatial proximity of luciferase-expressing cells to photosensitized blood vessels. Uniform vessel sensitization could leverage minimally

invasive gene delivery methods<sup>39</sup> or transgenic animals to express bPAC variants or alternative actuators<sup>40</sup> throughout large fields of view. This kind of approach could also go further to limit off-target expression of the photosensitizer, which we observed to some extent in our experiments. We showed that intraventricular injection of a Cre-dependent bPAC vector into an SM22 $\alpha$ -Cre transgenic mouse can indeed result in homogeneous and specific vascular expression across the brain, which could be essential for future applications. Compared with the current studies, spatial precision of subsequent BLUsH measurements might be further refined by using single vessel-level imaging<sup>41–43</sup> to estimate luminescence patterns at finer scale via tomographic reconstruction methods. The success of such strategies could depend on specifics of vascular distribution in different tissues.

Extensions of the BLUsH technique can include its generalization to detection of additional luminescent reporters, including chemiluminescent probes and alternative luciferases that sense cell signalling or other biological events<sup>35</sup>. Future applications could employ luciferin analogues engineered for better blood–brain barrier permeability or for multiplexed parallel detection of luciferase variants with different substrate selectivity<sup>44</sup>. BLUsH might even be adapted to permit detection of fluorophores, where unfocused excitation light could be delivered through scattering tissue, but high-resolution near-field imaging would be again performed using photosensitized blood vessels. Meanwhile, BLUsH detection could be performed using alternative deep-tissue imaging methods with complementary strengths, such as MRI with cerebral blood volume<sup>45</sup> or arterial spin labelling<sup>46</sup> contrast, functional ultrasound<sup>47</sup>, photoacoustic tomography<sup>48</sup> and high-resolution haemodynamic X-ray imaging methods<sup>49,50</sup>. With developments such as these, the BLUsH approach will permit the facile combination of diverse optical probes with virtually any imaging modality, on a scale that spans entire organs and organisms.

## Methods

### Plasmids

The codon-adapted synthetic genes encoding bPAC, GLucM23, sbGLuc and NanoLuc were purchased from Integrated DNA Technologies. All the plasmids for expression in bacterial and mammalian cells were constructed using the Golden Gate method<sup>51</sup> in pEF-ENTRA (Addgene number 17427) or gWiz backbones (Genlantis). The plasmids were produced in *Escherichia coli* (E. cloni 10G, Lucigen Corporation) grown in lysogeny broth medium supplemented with kanamycin. The plasmids for AAV production were generated by Virovek using respective synthetic genes.

### Mammalian cell culture

The CHO K1 cells and A7r5 VSMCs were purchased from Millipore-Sigma and cultured in 90% F10 or DMEM medium supplemented with 10% foetal bovine serum (FBS), 100 units per millilitre penicillin, and 100  $\mu$ g ml<sup>-1</sup> streptomycin. The HEK 293 FreeStyle cells were purchased from Thermo Fisher Scientific and grown in FreeStyle expression medium. The cells were frozen in freezing medium composed of 80% F10 medium, 10% FBS and 10% dimethylsulfoxide.

### Lentivirus production and cell line generation

The 293FT cells (Thermo Fisher) were seeded into six-well plates at 1 million cells per well and transfected using Lipofectamine 2000 (Life Technologies) according to instructions at subconfluence. Co-transfection of 0.5 mg pMD2.G, 1 mg psPAX2 and 1 mg of the previously described lentiviral plasmid<sup>14</sup> encoding Glo22F reporter<sup>52</sup> (Promega, Madison, WI) was performed with 6.25 ml Lipofectamine 2000 reagent. The virus-containing supernatant was collected after 48 and 72 h, filtered through 0.45  $\mu$ m filters and used for infection. The supernatants were stored at 4 °C for up to a week. A7r5 cells were seeded into 24-well plates at 5,000 cells per well in the presence of 4  $\mu$ g ml<sup>-1</sup> polybrene in 50% fresh medium and 50% viral supernatants containing Glo22F virus. The medium was replaced with fresh viral supernatants daily for



4 days. Selection was performed using both antibiotic resistance and fluorescent markers for each lentivirus. Beginning on day 3 after initial infection, 10 mg ml<sup>-1</sup> blasticidin and 1 mg ml<sup>-1</sup> puromycin (Life Technologies) were added to the medium for selection, and selection was continued until all cells expressed the appropriate fluorescent markers.

### In vitro characterization of luciferases

The testing of luciferases in bacteria was conducted by growing *E. coli* BL21 (MilliporeSigma) transformed with respective luciferase-encoding plasmids in lysogeny broth medium supplemented with kanamycin at 37 °C to an optical density at 600 nm (OD<sub>600</sub>) of 0.4. The expression of luciferase genes was induced by adding 1 mM isopropyl β-D-1-thiogalactopyranoside, and the cultures were grown overnight at 16 °C. The samples of similar cell density (250,000 cells in 200 μl) were taken for all cultures and transferred to 96-well plates. Bioluminescence was stimulated by addition of 10 μl of 2 mM CTZ (number 3031, CTZ-SOL, Nanolight Technology) to a final concentration of 95 μM or by addition of varying amounts for titration analysis. The resulting bioluminescence was recorded using a microwell luminescence reader, a power meter or IVIS Spectrum bioluminescence imaging system (Perkin Elmer). The testing in mammalian cells was conducted by transfecting HEK 293 FreeStyle cells with luciferase-encoding plasmids using 293fectin transfection reagent (Thermo Fisher). The luminescence was stimulated and measured as described above.

### cAMP cell assay

The production of intracellular cAMP was measured using the GloSensor assay<sup>52</sup> (Promega) in CHO K1 or A7r5 cells. Two days before the assay, 5,000 CHO cells or 2,000 A7r5 cells per well were seeded in 100 μl F10 or DMEM with 10% FBS in white opaque clear-bottom 96-well plates (Costar). After 24 h, the cells were transfected with bPAC-encoding plasmids using Lipofectamine (Thermo Fisher). Before the assay, the medium was removed from the wells and replaced with 90 μl per well of Gibco CO<sub>2</sub>-independent medium (Life Technologies) with 10% FBS containing 2% v/v of cAMP GloSensor substrate stock solution (Promega). The cells were incubated in substrate-containing medium at 37 °C in 5% CO<sub>2</sub> for 2–4 h and equilibrated to room temperature and atmospheric CO<sub>2</sub> for 30 min. The luminescence was measured for 30 min using a microtitre plate reader and evaluated after the signal reached a plateau (15 min).

### Animal procedures

All animal procedures were conducted in accordance with National Institutes of Health guidelines and with the approval of the Massachusetts Institute of Technology Committee on Animal Care (protocol number 0721-059-24). All rat experiments were performed with male Sprague–Dawley animals, 300–400 g, supplied by Charles River Laboratories. A total of 26 rats were used for the in vivo imaging experiments described here.

### Intracranial injection of viral vectors

The AAVs AAV9-SM22α-Cre-2A-GFP, AAV9-FLEX-CAG-bPAC-Myc-2A-mCherry and AAV9-CAG-GLucM23-HA were custom ordered from Virovek. AAV9-CAG-FLEX-tdTomato was purchased from Addgene (number 28306). The animals were anaesthetized with isoflurane (4% for induction and 2% for maintenance) and positioned in a stereotaxic instrument (Kopf Instruments) with a water heating pad (Braintree Scientific) to keep the body temperature at 37 °C. The animals' eyes were covered with Paralube Vet Ointment (Dechra Veterinary Products) to prevent drying, and the heads were shaved and cleaned with alcohol and povidone–iodine pads. Using sterile surgical equipment, the skin over the skull was retracted and the skull cleaned to expose the target virus injection sites. Holes were drilled into the skull above the target sites, which were located in the cortex (AP +1 mm; ML ± 2.5 mm, DV 0.5 mm) for imaging photosensitized vasculature or the central

striatum (AP 0; ML ± 3 mm, DV 5 mm) for BLUSH imaging of xenografts and optical reporter expression.

A glass pipette preloaded with appropriate viral vectors at final concentrations of 10<sup>12</sup> vg ml<sup>-1</sup> was lowered into the brain, and the viral vectors were injected into the brain parenchyma. The animals for imaging photosensitized vasculature and BLUSH imaging of xenografts were injected with a total volume of 1.5 μl of AAV9-SM22α-Cre-2A-GFP and AAV9-FLEX-CAG-bPAC-Myc-2A-mCherry at a 1:1 ratio. The animals for BLUSH imaging of optical reporter expression were injected with a total volume of 3 μl of AAV9-SM22α-Cre-2A-GFP, AAV9-FLEX-CAG-bPAC-Myc-2A-mCherry and AAV9-CAG-GLucM23-HA at a 1:1:1 ratio. The glass pipette was slowly removed 10 min after the viral injection. Bone wax was applied to each injection site using a sterile cotton applicator tip. The skin incisions were closed using surgical suture, and lidocaine gel (2%) was applied over the wound areas. Isoflurane was then discontinued, and each rat was removed from the stereotaxic frame and placed in a warmed cage on a heating pad to recover for 45 min. Slow-release buprenorphine (0.3 mg kg<sup>-1</sup>, Massachusetts Institute of Technology pharmacy) was administered subcutaneously to minimize pain and discomfort. To verify the feasibility of achieving brain-wide homogeneous bPAC expression, a small number of SM22α-Cre transgenic mice<sup>53</sup> (number 017491, Jackson Laboratory) underwent bilateral injection of 3 μl AAV.PHP.eB-FLEX-CAG-bPAC-Myc-2A-mCherry (Boston Children's Hospital, 6 × 10<sup>13</sup> vg ml<sup>-1</sup>) each into the ventricles, using procedures described above. Following standard practices in the field, a delay of 6 weeks between AAV infection and further experiments was instituted to allow AAV-mediated expression to develop.

### Implantation of luminescent xenografts

HEK 293 FreeStyle cells transiently expressing GLucM23 as described above were collected 48 h after transfection, pelleted by centrifugation, washed with cold phosphate-buffered saline (PBS, pH 7.4) and resuspended at a density of 10<sup>5</sup> cells per microlitre in artificial cerebrospinal fluid. Six weeks after viral injection (AAV9-SM22α-Cre-2A-GFP and AAV9-FLEX-CAG-bPAC-Myc-2A-mCherry or AAV9-FLEX-CAG-mCherry), immediately before the BLUSH experiment, GLucM23-expressing xenografts were intracranially implanted. Each animal was anaesthetized and prepared for stereotaxic surgery. Holes were drilled into the skull above the target sites (AP 0 mm, ML ± 3 mm) as described above; then, 28G PEEK cannula guides (Plastics One) designed to project 1 mm below the surface of the skull were lowered through the holes. The guides were fixed in place using SEcure light-curing dental cement (Parkell). A custom-fabricated plastic headpost was placed in front of the guide cannula and also secured with dental cement (Parkell). To deliver cells, 33G metal internal cannulas (Plastics One) were lowered through the guide cannulas to a depth of 5.5 mm below the skull. Approximately 5 × 10<sup>5</sup> GLucM23-expressing cells (5 μl) were infused to the bPAC-expressing brain hemispheres, control hemispheres or naive brain regions via the cannulas at a flow rate of 0.2 μl min<sup>-1</sup> for 25 min. The internal cannulas were slowly removed 10 min after the infusion. The cannula guides were then sealed with dummy cannulas.

### Functional MRI of photosensitized vasculature

The animals were anaesthetized with isoflurane (4% for induction and 2% for maintenance). Small cranial windows of around 1 mm<sup>2</sup> were prepared above the respective virus injection sites and over more caudal control sites where no virus was administered. The animals were then transferred to a 9.4 T MRI scanner (Bruker Instruments) and fixed into a custom rat MRI cradle. The isoflurane was discontinued, and the animals were sedated with intraperitoneal medetomidine (bolus of 0.1 mg kg<sup>-1</sup>, followed by 0.1 mg per kilogram per hour infusion). An optical fibre of 200 μm diameter coupled to a blue LED (470 nm from NPI Electronic) was mounted on top of each cranial window to provide light illumination with output intensities of 0.1, 0.5 and 1.0 mW cm<sup>-2</sup>, as measured using a light power meter at the fibre tip.



The cranial windows were then sealed with silicone gel. A transmit-only 70-cm-inner-diameter linear volume coil (Bruker) and a three-channel surface receive-only radiofrequency coil (Bruker) were used for image acquisition.

The scanner operation was controlled using the ParaVision 6.1 software (Bruker). Field map shimming was performed to optimize main field homogeneity. High-resolution anatomical MRI images were acquired using a longitudinal relaxation time ( $T_2$ )-weighted rapid acquisition with refocused echoes pulse sequence with a factor of 8, bandwidth of 200 kHz, effective echo time of 30 ms, repetition time of 5 s, in-plane field of view of  $2.56 \times 2.56 \text{ cm}^2$ , in-plane resolution of  $100 \times 100 \mu\text{m}^2$  and slice thickness of 1 mm. Functional imaging scan series were acquired using a standard gradient echo EPI pulse sequence with echo time values of 20 ms, flip angle of  $90^\circ$ , repetition time of 2 s, field of view of  $2.56 \times 2.56 \text{ cm}^2$  and in-plane resolution of  $400 \times 400 \mu\text{m}^2$  with a slice thickness of 1 mm. EPI MRI scans were continuously collected for 2 min of baseline, for 1 min during illumination and for 7 min after illumination. The animals were warmed using a water heating pad (Braintree). The heart rate and blood oxygenation saturation level were continuously monitored using an MRI-compatible infra-red pulse oximeter (Nonin Medical). The breathing rate and  $\text{CO}_2$  level were continuously monitored using an MRI-compatible SurgiVet  $\text{CO}_2$  monitor (Smiths Medical).

MRI images were reconstructed using the ParaVision 6.1 software and further processed using the AFNI software package<sup>54</sup>. High-resolution anatomical images were registered based on the location of cranial windows at each stimulation site, such that all test or control stimulation sites were positioned on the righthand side after alignment, using left–right reflection where needed. Time series of  $T_2^*$ -weighted EPI images were pre-processed in steps that included slice timing correction, motion correction using a least-squares rigid-body volume registration algorithm, voxel-wise intensity normalization, spatial smoothing with Gaussian spatial kernel of 0.5 mm full width at half maximum and spatial resampling to double the image matrix size, all implemented in AFNI. The segmentation of brain from non-brain voxels was performed in MATLAB (MathWorks). The pre-processed time series were then co-registered onto the previously aligned anatomical images. The response maps were computed as mean per cent signal change during the expected peak response timepoint, 0–40 s after the onset of light illumination, minus the average baseline signal 40–120 s before stimulus onset. The mean response maps from aligned stimulated hemispheres were overlaid on full coronal anatomical MRI slices to produce panels in Fig. 2d.

The mean response amplitudes and time courses were evaluated over ROIs defined with respect to fibre tips estimated from the MRI scans. Time courses were baseline corrected using the initial and final 50 timepoints and are presented as mean and standard error of the mean (s.e.m.) over animals. The amplitudes were defined as the mean per cent signal change observed from 40–80 s after stimulus onset, with respect to baseline signal 20–60 s before onset. The depth profiles represent mean amplitudes measured at 200- $\mu\text{m}$  depth increments from the fibre tip locations. The rate constants for response to and recovery from optical stimulation were estimated by fitting mono-exponential curves to the first 120 s after stimulus onset or the first 360 s after stimulus offset, respectively.

### BLUsH imaging of luminescent xenografts

After implantation of GLucM23-expressing cells, the internal metal cannulas were removed. The animals were then transferred to the scanner and placed in the cradle, and 33G PEEK internal cannulas (Plastics One) were connected to PE-50 tubing (Plastics One) loaded with CTZ (2 mM) and lowered through the guide cannulas to the same site for cells implantation at a depth of 5.5 mm below the skull. The animals were anaesthetized, sedated and monitored as described above and paralysed with pancuronium (intraperitoneal bolus of  $1 \text{ mg kg}^{-1}$ , followed by

$1 \text{ mg per kilogram per hour}$  infusion). Intubation and ventilation were conducted with a small animal ventilator (Harvard Apparatus), which operated at 62 beats per minute with a 6 ml stroke volume, delivering oxygen and air as a 5:1 ratio mixture. General MRI methods, including hardware, anatomical imaging and functional  $T_2^*$ -weighted imaging, were similar to those described above. The EPI MRI scans were continuously collected for 5 min of baseline, for 5 min during CTZ infusion and for 20 min of resting after the infusion. Intracranial CTZ infusion was produced by infusion of a 2 mM solution of CTZ in Ringer's solution at a rate of  $0.2 \mu\text{l min}^{-1}$  through the internal cannulas.

MRI images were reconstructed and pre-processed as described above. High-resolution anatomical images of each animal were registered to a Waxholm coordinate space rat brain atlas<sup>55</sup> using AFNI, again such that implant sites were positioned on the righthand side. MATLAB codes were used for the rest of the analysis. The response maps were computed as mean per cent signal change during the expected peak response timepoint, 1–120 s after the onset of CTZ infusion minus the average baseline signal 20–200 s before infusion. The average response maps from xenografts in aligned hemispheres were overlaid on full coronal anatomical MRI slices to produce panels in Fig. 3b.

The mean response amplitudes and time courses were evaluated over an ROI around the cell implantation area. These ROIs were defined by  $1.6 \text{ mm} \times 1.2 \text{ mm}$  ROIs defined around cannula tip locations in individual animals' datasets, and the standard error was calculated across animals. The closeup average per cent signal change and corresponding standard deviation maps were computed by combining data from  $3.8 \text{ mm} \times 3.8 \text{ mm}$  squares defined around the centroid of CTZ-induced MRI signal change in each experiment. Full widths at half maximum were computed from interpolated cross sections at the dorsolateral median of each response. A model of the expected BLUsH signal through the median of a 1-mm-diameter spherical xenograft was generated by computing the one-dimensional projection of a circular cross section and smoothing it by a Gaussian function to simulate the MRI data processing.

The CTZ dose–response curves for the xenograft BLUsH experiments were generated by comparing effective CTZ concentrations to the mean MRI response amplitudes in volumes approximately corresponding to the closeup analysis of BLUsH signal changes in Fig. 3c. Effective [CTZ] values were estimated by dividing the total injected amount of CTZ at varying timepoints by a  $58 \mu\text{l}$  volume ( $11 \times 11 \times 3$  voxels) centred around the centroid of maximal CTZ-induced MRI signal change in each experiment. The mean BLUsH response amplitudes were computed over the same volumes at the same timepoints used for [CTZ] estimation.

### Consideration of $\text{CO}_2$ effects

To investigate responses to  $\text{CO}_2$ -induced vasodilation, two further animals underwent MRI at 7 T under conditions otherwise equivalent to the xenograft BLUsH experiments of Fig. 3 but during challenge with inhaled carbogen ( $90\% \text{ CO}_2$ ,  $10\% \text{ O}_2$ ) in place of CTZ injection. The response maps were computed as the per cent difference between the mean EPI signal in the 20 s after carbogen-induced monotonic signal increases versus mean signal in the 20 s before carbogen response. An estimated upper bound on  $\text{CO}_2$  production and  $\text{O}_2$  consumption rates in the xenograft experiments was based on the infusion parameters of 2 mM CTZ at  $0.2 \mu\text{l min}^{-1}$  over  $5 \mu\text{l}$  ( $\sim 5 \text{ mg}$ ) of cells. Assuming optimistically that all CTZ is instantaneously converted, this implies  $\text{O}_2$  consumption and  $\text{CO}_2$  generation rates of  $0.1 \mu\text{mol per gram (cells) per minute}$ .

### BLI of luminescent xenografts

HEK 293 FreeStyle cells transiently expressing GLucM23 or the red-shifted luciferase Akaluc were collected 48 h after transfection, pelleted by centrifugation, washed with cold PBS (pH 7.4) and resuspended at a density of  $10^5 \text{ cells } \mu\text{l}^{-1}$  in artificial cerebrospinal fluid. The luminescence of the cells when exposed to the substrates CTZ (for GLucM23)

and the luciferin analogue AkaLumine (for Akaluc) was confirmed by imaging transfected cells in a microtitre plate using a high-sensitivity camera (iXon Life 897 EMCCD, Andor USA) in a custom-fabricated chamber. Four animals then underwent a craniotomy and approximately  $5 \times 10^5$  luminescent cells were implanted into each animal via a 26G Hamilton syringe at a flow rate of  $0.2 \mu\text{L min}^{-1}$  for 25 min, targeting the same coordinates used for MRI studies. Two animals received GLucM23 cells and two received Akaluc cells. Using a Hamilton syringe,  $8 \mu\text{L}$  of 5 mM CTZ or  $8 \mu\text{L}$  of 6.2 mM AkaLumine were infused at a rate of  $2 \mu\text{L min}^{-1}$  over the corresponding implanted xenografts before withdrawal of the infusion needle. The scalp was sutured over the implantation site, and the animals were immediately imaged using the camera, with exposure parameters for GLucM23 of 100 gain with 1 s exposure and for Akaluc of 100 gain with 30 s exposure. The values are presented as two-dimensional plots of luminescence in arbitrary units superimposed on brightfield images. The FWHM values were computed from Gaussian fitting of the cross section with brightest luminescence signal.

### BLUsH imaging of virally driven optical reporter expression

MRI imaging was performed 6 weeks after viral injection. The animals were anaesthetized, sedated and continuously monitored during imaging as described above. General MRI imaging hardware, anatomical imaging and functional  $T_2^*$ -weighted imaging were the same as the section above. CTZ (250  $\mu\text{L}$  at 2 mM) was administered systemically via the tail vein. EPI scans were continuously collected before, during and after the administration of CTZ. The MRI images were reconstructed, pre-processed and registered the same way as described above, with treatment sites all on the righthand side after alignment. The peak BLUsH MRI signals were observed up to 25 min after CTZ injection. The response maps were computed as mean per cent signal change observed over a time window of 40 s, starting at the peak signal change, minus the average baseline signal observed 100–200 s before the peak. The mean response amplitudes and time courses were evaluated over an ROI of  $3 \times 3$  voxels around the maximum signal change. The peak signal changes were quantified as the maximal signal amplitude in each test and control animal with respect to an average baseline 100–200 s before the peak signal.

Correspondence between BLUsH and histology images was assessed after aligning GLucM23 histology images from each of three animals to the corresponding single-slice BLUsH MRI images, as judged by eye. An affine alignment was performed using the ‘imwarp’ command in MATLAB, with landmarks chosen manually around cortical features and ventricles. The data were smoothed along both dimensions with a Gaussian of window size of 6.4 mm. The correlations and linear regression parameters were computed by comparing BLUsH signal amplitudes and normalized GLucM23 fluorescence ( $F/F_{\text{max}}$ ) of the resulting aligned, smoothed images for each of the three animals.

### Histology

The animals were transcardially perfused with PBS followed by 4% paraformaldehyde in PBS. The brains were extracted, post-fixed overnight at  $4^\circ\text{C}$  and sectioned the following day. Free-floating sections (50  $\mu\text{m}$  thick) were cut using a vibratome (Leica VT1200 S, Leica Microsystems GmbH). We performed antigen retrieval by incubating brain sections in sodium citrate buffer (pH 6) for 30 min at  $80^\circ\text{C}$ .

Expression of bPAC, fluorescent control proteins and GLucM23 were assessed by overnight incubation with primary antibodies anti-mCherry (1:250 dilution, LS-C204207, Lifespan Biosciences), anti-tdTomato (1:250 dilution, LS-C340696, Lifespan Biosciences) and anti-HA (1:250 dilution, NB600-363, Novus Biologicals), followed by a 1 h incubation with matching secondary antibodies anti-Goat Alexa Fluor 594 (1:500 dilution, ab150132, Abcam) and anti-Rabbit Alexa Fluor 405 (1:500 dilution, ab175651, Abcam). The cell implants expressing GLucM23 were stained using anti-His (1:250 dilution,

MA5-33032, Invitrogen) primary and anti-Rabbit Alexa Fluor 405 secondary antibodies.

Microglial activation in BLUsH brain slices was assessed using 2-day incubation with primary antibodies anti-mCherry (1:500 dilution, ab205402, Abcam), anti-HA (1:500 dilution, ab9110, Abcam) and anti-Iba1 (1:500 dilution, ab5076, Abcam), followed by a 3-h incubation with matching secondary antibodies anti-Chicken Alexa Fluor 647 (1:500 dilution, A78952, Invitrogen), anti-Rabbit Rhodamine Red (1:200 dilution, 711-295-152, Jackson ImmunoResearch) and anti-Goat Alexa Fluor 488 (1:500 dilution, 705-545-003, Jackson ImmunoResearch). Inflammation markers were assessed using anti-nitrotyrosine (1:200 dilution, MilliporeSigma AB5411) with secondary antibody anti-Rabbit Alexa Fluor 405 (1:500 dilution, ab175651, Abcam). The vascular staining was performed by overnight incubation of brain sections with Tomato Lectin DyLight488 (1:250 dilution, DL-1174, Vector Laboratories).

The stained brain sections were mounted on glass slides with Invitrogen ProLong Gold Antifade (Fisher Scientific Company) and protected with a coverslip. Fluorescence imaging was performed using a confocal microscope (Axio Imager 2, Zeiss).

### Reporting summary

Further information on research design is available in the Nature Portfolio Reporting Summary linked to this article.

### Data availability

The main data supporting the results in this study are available within the paper and its Supplementary Information. The MRI atlas used for this study was downloaded from NITRC via <https://www.nitrc.org/projects/whs-sd-atlas> (ref. 55). The raw and analysed datasets generated during the study are available for research purposes from the corresponding author on reasonable request. Source data are provided with this paper.

### References

1. Yeh, H. W. & Ai, H. W. Development and applications of bioluminescent and chemiluminescent reporters and biosensors. *Annu. Rev. Anal. Chem.* **12**, 129–150 (2019).
2. Liu, S., Su, Y., Lin, M. Z. & Ronald, J. A. Brightening up biology: advances in luciferase systems for in vivo imaging. *ACS Chem. Biol.* **16**, 2707–2718 (2021).
3. Dothager, R. S. et al. Advances in bioluminescence imaging of live animal models. *Curr. Opin. Biotechnol.* **20**, 45–53 (2009).
4. Tung, J. K., Berglund, K., Gutekunst, C. A., Hochgeschwender, U. & Gross, R. E. Bioluminescence imaging in live cells and animals. *Neurophotonics* **3**, 025001 (2016).
5. Tian, X. et al. A luciferase prosubstrate and a red bioluminescent calcium indicator for imaging neuronal activity in mice. *Nat. Commun.* **13**, 3967 (2022).
6. Wang, G., Li, Y. & Jiang, M. Uniqueness theorems in bioluminescence tomography. *Med. Phys.* **31**, 2289–2299 (2004).
7. Gu, X., Zhang, Q., Larcum, L. & Jiang, H. Three-dimensional bioluminescence tomography with model-based reconstruction. *Opt. Express* **12**, 3996–4000 (2004).
8. Tu, C. & Louie, A. Y. Photochromically-controlled, reversibly-activated MRI and optical contrast agent. *Chem. Commun.* **13**, 1331–1333 (2007).
9. Osborne, E. A., Jarrett, B. R., Tu, C. & Louie, A. Y. Modulation of  $T_2$  relaxation time by light-induced, reversible aggregation of magnetic nanoparticles. *J. Am. Chem. Soc.* **132**, 5934–5935 (2010).
10. Venkataramani, S. et al. Magnetic bistability of molecules in homogeneous solution at room temperature. *Science* **331**, 445–448 (2011).

11. Hai, A., Spanoudaki, V. C., Bartelle, B. B. & Jasanoff, A. Wireless resonant circuits for the minimally invasive sensing of biophysical processes in magnetic resonance imaging. *Nat. Biomed. Eng.* **3**, 69–78 (2019).
12. Reessing, F. et al. A light-responsive liposomal agent for MRI contrast enhancement and monitoring of cargo delivery. *Chem. Commun.* **55**, 10784–10787 (2019).
13. Simon, J., Schwalm, M., Morstein, J., Trauner, D. & Jasanoff, A. Mapping light distribution in tissue by using MRI-detectable photosensitive liposomes. *Nat. Biomed. Eng.* **7**, 313–322 (2023).
14. Ohlendorf, R. et al. Target-responsive vasoactive probes for ultrasensitive molecular imaging. *Nat. Commun.* **11**, 2399 (2020).
15. Desai, M., Slusarczyk, A. L., Chapin, A., Barch, M. & Jasanoff, A. Molecular imaging with engineered physiology. *Nat. Commun.* **7**, 13607 (2016).
16. Desai, M. et al. Hemodynamic molecular imaging of tumor-associated enzyme activity in the living brain. *eLife* **10**, e70237 (2021).
17. Ghosh, S. et al. Functional dissection of neural circuitry using a genetic reporter for fMRI. *Nat. Neurosci.* **25**, 390–398 (2022).
18. Ji, X. et al. Brain microvasculature has a common topology with local differences in geometry that match metabolic load. *Neuron* **109**, 1168–1187.e13 (2021).
19. Farhadi, A., Sigmund, F., Westmeyer, G. G. & Shapiro, M. G. Genetically encodable materials for non-invasive biological imaging. *Nat. Mater.* **20**, 585–592 (2021).
20. Attwell, D. et al. Glial and neuronal control of brain blood flow. *Nature* **468**, 232–243 (2010).
21. Walsh, M. P. & Cole, W. C. The role of actin filament dynamics in the myogenic response of cerebral resistance arteries. *J. Cereb. Blood Flow Metab.* **33**, 1–12 (2013).
22. Hillman, E. M. Coupling mechanism and significance of the BOLD signal: a status report. *Annu. Rev. Neurosci.* **37**, 161–181 (2014).
23. Stierl, M. et al. Light modulation of cellular cAMP by a small bacterial photoactivated adenylyl cyclase, bPAC, of the soil bacterium *Beggiatoa*. *J. Biol. Chem.* **286**, 1181–1188 (2011).
24. Berglund, K. et al. Combined optogenetic and chemogenetic control of neurons. *Methods Mol. Biol.* **1408**, 207–225 (2016).
25. Hall, M. P. et al. Engineered luciferase reporter from a deep sea shrimp utilizing a novel imidazopyrazinone substrate. *ACS Chem. Biol.* **7**, 1848–1857 (2012).
26. Park, S. Y. et al. Novel luciferase-opsin combinations for improved luminopsins. *J. Neurosci. Res.* **98**, 410–421 (2020).
27. Stuenkel, B. et al. Characterization and engineering of photoactivated adenylyl cyclases. *Biol. Chem.* **400**, 429–441 (2019).
28. Moessler, H. et al. The SM 22 promoter directs tissue-specific expression in arterial but not in venous or visceral smooth muscle cells in transgenic mice. *Development* **122**, 2415–2425 (1996).
29. Chakraborty, R. et al. Promoters to study vascular smooth muscle. *Arterioscler. Thromb. Vasc. Biol.* **39**, 603–612 (2019).
30. Deverman, B. E. et al. Cre-dependent selection yields AAV variants for widespread gene transfer to the adult brain. *Nat. Biotechnol.* **34**, 204–209 (2016).
31. Han, S., Son, J. P., Cho, H., Park, J. Y. & Kim, S. G. Gradient-echo and spin-echo blood oxygenation level-dependent functional MRI at ultrahigh fields of 9.4 and 15.2 tesla. *Magn. Reson. Med.* **81**, 1237–1246 (2019).
32. Grandjean, J. et al. A consensus protocol for functional connectivity analysis in the rat brain. *Nat. Neurosci.* **26**, 673–681 (2023).
33. Abe, Y. et al. Optical manipulation of local cerebral blood flow in the deep brain of freely moving mice. *Cell Rep.* **36**, 109427 (2021).
34. Iwano, S. et al. Single-cell bioluminescence imaging of deep tissue in freely moving animals. *Science* **359**, 935–939 (2018).
35. Wang, A., Feng, J., Li, Y. & Zou, P. Beyond fluorescent proteins: hybrid and bioluminescent indicators for imaging neural activities. *ACS Chem. Neurosci.* **9**, 639–650 (2018).
36. Ntziachristos, V. Going deeper than microscopy: the optical imaging frontier in biology. *Nat. Methods* **7**, 603–614 (2010).
37. Wiesner, H. M. et al. Quantitative and simultaneous measurement of oxygen consumption rates in rat brain and skeletal muscle using  $^{17}\text{O}$  MRS imaging at 16.4T. *Magn. Reson. Med.* **85**, 2232–2246 (2021).
38. Ueda, H. R. et al. Tissue clearing and its applications in neuroscience. *Nat. Rev. Neurosci.* **21**, 61–79 (2020).
39. Bedbrook, C. N., Deverman, B. E. & Gradinaru, V. Viral strategies for targeting the central and peripheral nervous systems. *Annu. Rev. Neurosci.* **41**, 323–348 (2018).
40. Rost, B. R., Schneider-Warme, F., Schmitz, D. & Hegemann, P. Optogenetic tools for subcellular applications in neuroscience. *Neuron* **96**, 572–603 (2017).
41. Yu, X. et al. Sensory and optogenetically driven single-vessel fMRI. *Nat. Methods* **13**, 337–340 (2016).
42. Renaudin, N. et al. Functional ultrasound localization microscopy reveals brain-wide neurovascular activity on a microscopic scale. *Nat. Methods* **19**, 1004–1012 (2022).
43. Zhu, X. et al. Real-time whole-brain imaging of hemodynamics and oxygenation at micro-vessel resolution with ultrafast wide-field photoacoustic microscopy. *Light. Sci. Appl.* **11**, 138 (2022).
44. Zambito, G., Chawda, C. & Mezzanotte, L. Emerging tools for bioluminescence imaging. *Curr. Opin. Chem. Biol.* **63**, 86–94 (2021).
45. Belliveau, J. W. et al. Functional cerebral imaging by susceptibility-contrast NMR. *Magn. Reson. Med.* **14**, 538–546 (1990).
46. Williams, D. S., Detre, J. A., Leigh, J. S. & Koretsky, A. P. Magnetic resonance imaging of perfusion using spin inversion of arterial water. *Proc. Natl Acad. Sci. USA* **89**, 212–216 (1992).
47. Mace, E. et al. Functional ultrasound imaging of the brain. *Nat. Methods* **8**, 662–664 (2011).
48. Wang, L. V. & Hu, S. Photoacoustic tomography: in vivo imaging from organelles to organs. *Science* **335**, 1458–1462 (2012).
49. Hayasaka, N. et al. In vivo diagnostic imaging using micro-CT: sequential and comparative evaluation of rodent models for hepatic/brain ischemia and stroke. *PLoS ONE* **7**, e32342 (2012).
50. Starosolski, Z. et al. Ultra high-resolution in vivo computed tomography imaging of mouse cerebrovasculature using a long circulating blood pool contrast agent. *Sci. Rep.* **5**, 10178 (2015).
51. Engler, C., Kandzia, R. & Marillonnet, S. A one pot, one step, precision cloning method with high throughput capability. *PLoS ONE* **3**, e3647 (2008).
52. Fan, F. et al. Novel genetically encoded biosensors using firefly luciferase. *ACS Chem. Biol.* **3**, 346–351 (2008).
53. Holtwick, R. et al. Smooth muscle-selective deletion of guanylyl cyclase-A prevents the acute but not chronic effects of ANP on blood pressure. *Proc. Natl Acad. Sci. USA* **99**, 7142–7147 (2002).
54. Cox, R. W. AFNI: software for analysis and visualization of functional magnetic resonance neuroimages. *Comput. Biomed. Res.* **29**, 162–173 (1996).
55. Papp, E. A., Leergaard, T. B., Calabrese, E., Johnson, G. A. & Bjaalie, J. G. Waxholm Space atlas of the Sprague Dawley rat brain. *Neuroimage* **97**, 374–386 (2014).

## Acknowledgements

We acknowledge grants to A.J. from the National Institutes of Health (UG3 MH126868, U01 EBO31641, R21 EYO32369 and R01



NS121073) and the G. Harold and Leila Y. Mathers Foundation. We also gratefully acknowledge research funding from L. McGovern, G. Hendrie and B. Fikes. R.O. was funded by a fellowship from the Deutsche Forschungsgemeinschaft. M.S. was funded by a Marie Skłodowska-Curie fellowship from the European Union. Y.K. was supported by a Y. Eva Tan Fellowship, and Y.J. was supported by a J. Douglas Tan Fellowship, both from the McGovern Institute for Brain Research. A. Becker and K. Backman are thanked for technical support.

### Author contributions

R.O. and A.J. designed the BLUsH principle. R.O. performed most of the in vitro experiments. N.L. and R.O. performed the in vivo MRI experiments with contributions from V.D.P.V., M.S., M.D. and W.T.Z. R.O., V.D.P.V., Y.K. and B.S. performed histology analyses. Y.K. and Y.J. performed the BLI experiments. S.D. performed the in vitro CTZ titration. N.L., R.O. and A.J. analysed the imaging data. R.O., N.L. and A.J. wrote the paper.

### Competing interests

The authors declare no competing interests.

### Additional information

**Extended data** is available for this paper at <https://doi.org/10.1038/s41551-024-01210-w>.

**Supplementary information** The online version contains supplementary material available at <https://doi.org/10.1038/s41551-024-01210-w>.

**Correspondence and requests for materials** should be addressed to Alan Jasanoff.

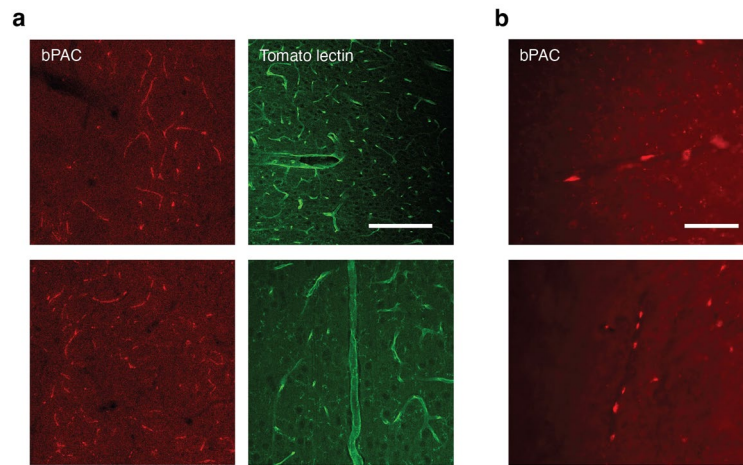
**Peer review information** *Nature Biomedical Engineering* thanks Ge Wang and the other, anonymous, reviewer(s) for their contribution to the peer review of this work.

**Reprints and permissions information** is available at [www.nature.com/reprints](http://www.nature.com/reprints).

**Publisher's note** Springer Nature remains neutral with regard to jurisdictional claims in published maps and institutional affiliations.

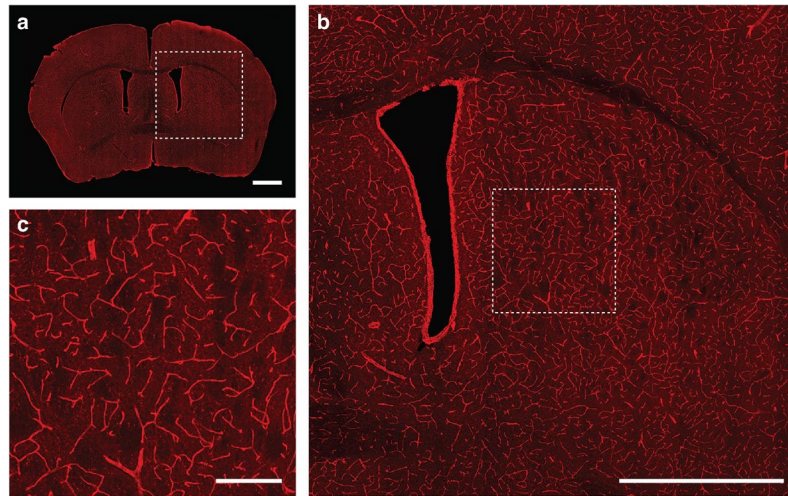
Springer Nature or its licensor (e.g. a society or other partner) holds exclusive rights to this article under a publishing agreement with the author(s) or other rightsholder(s); author self-archiving of the accepted manuscript version of this article is solely governed by the terms of such publishing agreement and applicable law.

© The Author(s), under exclusive licence to Springer Nature Limited 2024



**Extended Data Fig. 1 | Vascular expression of bPAC.** (a) Expression of bPAC (red, left) in two fields of view (top and bottom), compared with the tomato lectin vascular stain (green, right) in two fields of view from a different animal, showing

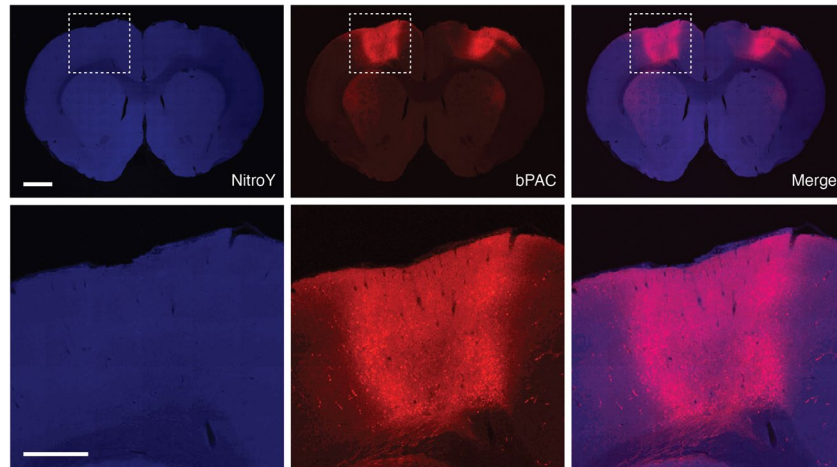
similarity of labeled features as in Fig. 2b. Scale bar = 200  $\mu\text{m}$ . (b) Images showing bPAC expression in individual cells spaced along individual vessels, analogous to Fig. 2c. Scale bars = 100  $\mu\text{m}$  (top) and 200  $\mu\text{m}$  (bottom).



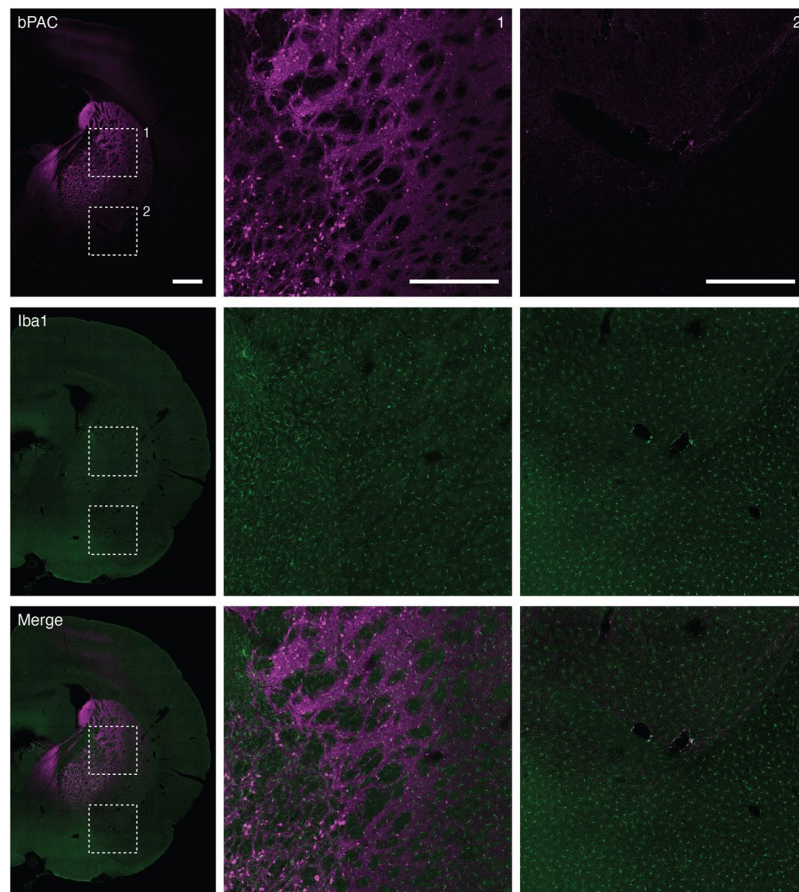
**Extended Data Fig. 2 | Brain-wide vascular expression of bPAC in transgenic mouse.** (a) Immunohistochemical visualization of bPAC expression in a coronal slice from a representative SM22 $\alpha$ -Cre transgenic mouse infected with a Cre-

activated bPAC vector, showing strong and homogeneous labeling of brain-wide vasculature in the slice. Scale bar = 1 mm. (b) Close-up of the boxed region in a. Scale bar = 1 mm. (c) Close-up of the boxed region in b. Scale bar = 100  $\mu$ m.



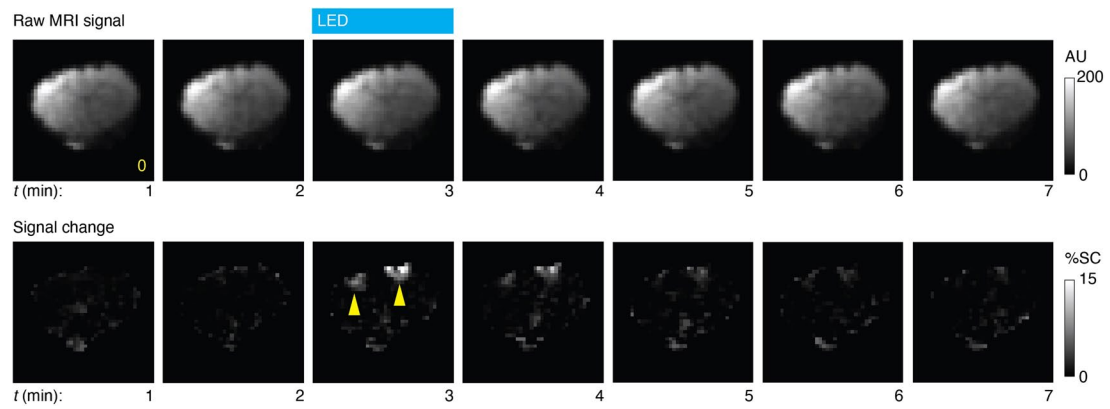


**Extended Data Fig. 3 | Analysis of nitrotyrosine accumulation.** Nitrotyrosine (NitroY) staining (blue, left) was performed to examine whether elevations of this marker colocalize with bPAC expression (red, middle) in virally transduced rat brain regions. Merged image is shown at right. Scale bars = 1 mm (top) and 500  $\mu$ m (bottom).

**Extended Data Fig. 4 | Microglial staining in bPAC-expressing tissue.**

Comparison of bPAC expression profile (top) with distribution of the microglial marker Iba1 (middle) and overlay (bottom), showing absence of clear microglial activation in bPAC-rich areas in a representative BLUsH-treated

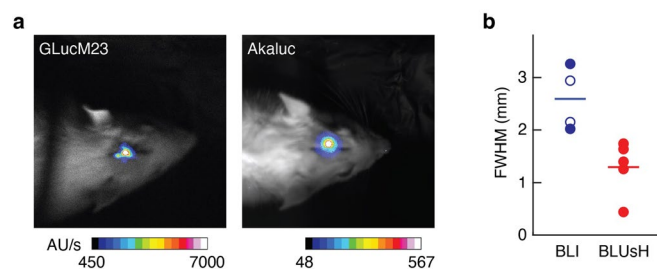
brain hemisphere. Panels at right represent enlargements of the dashed areas in the panels at left. Areas 1 and 2 were chosen to be regions with and without substantial bPAC expression, respectively. Scale bars = 1 mm (left) or 500  $\mu$ m (right).

**Extended Data Fig. 5 | Raw time series data during light stimulation.**

Individual image frames from an experiment as in Fig. 2d, showing raw MRI scans (top) and signal changes from baseline (bottom) at time points ( $t$ ) relative to the beginning of the experiment, denoted in minutes below each frame. Grey

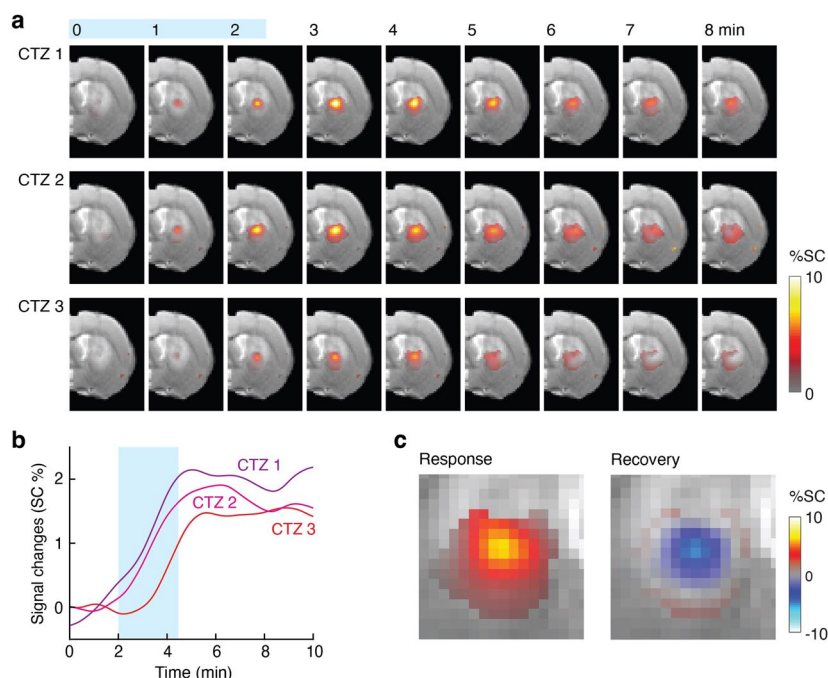
scales denote arbitrary intensity units (AU, top) or percent signal change (%SC, bottom). The onset of signal changes coincident with bilateral LED illumination (blue bar) is indicated by the yellow arrowheads.





**Extended Data Fig. 6 | BLI of luciferase-expressing xenografts.** (a) BLI signal (color) and reflectance images (grayscale) of individual rats implanted with bioluminescent xenografts prepared and implanted as for the experiments of Fig. 3. The implant in the left animal expressed GLucM23, as in Fig. 3, while the implant in the rat on the right expressed Akaluc, a red-shifted luciferase.

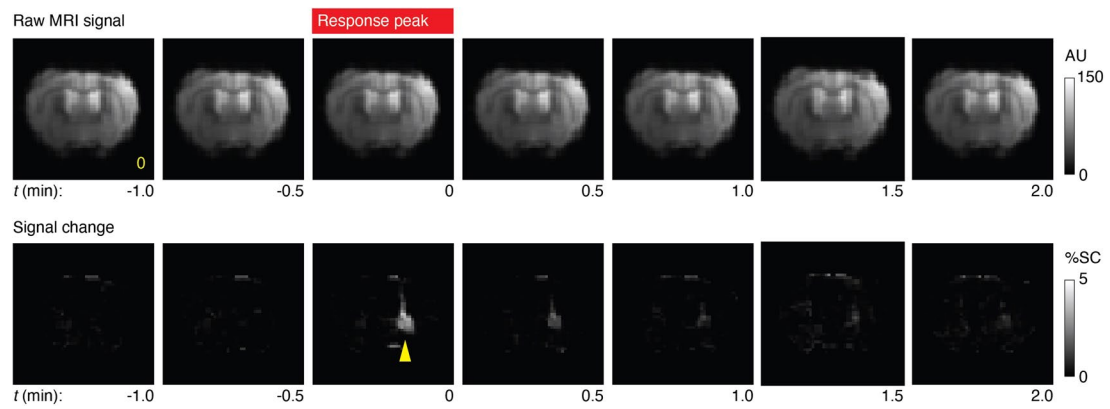
(b) FWHM of luminescence signals measured by BLI (closed purple circles = GLucM23, open purple circles = Akaluc), compared with values measured by MRI-based BLUsH (red circles). Horizontal lines denote means for BLI and BLUsH data points. The difference between BLI and BLUsH size measurements is significant with  $t$ -test  $p = 0.01$ ,  $n = 4, 5$ .



**Extended Data Fig. 7 | BLUSH responses to repeated CTZ administration.**

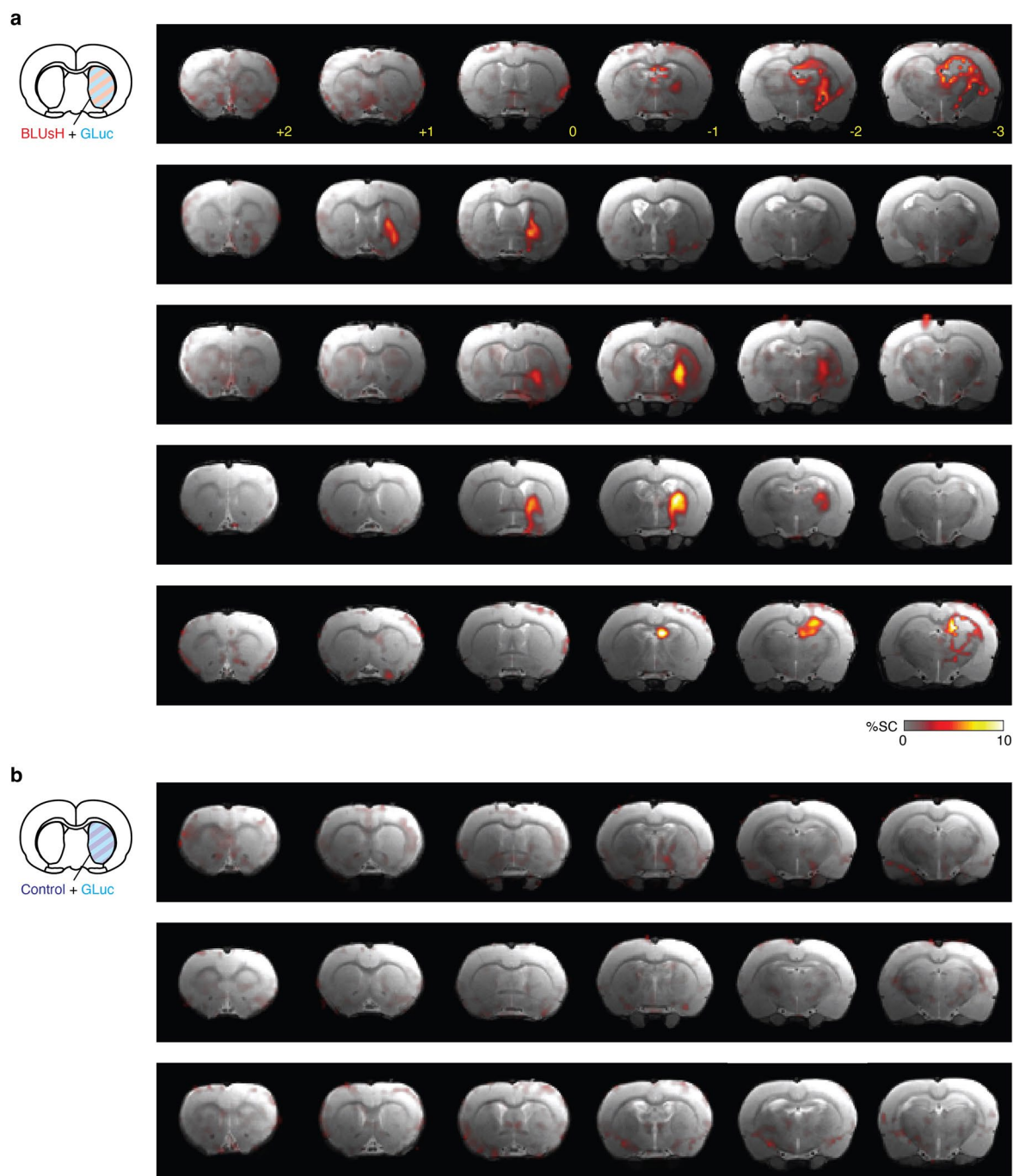
**(a)** Snapshots of the responses to three doses of CTZ infused over a luciferase-expressing cell pellet in a single animal, following the experimental paradigm of Fig. 3. CTZ was injected in 2.5-min epochs (blue shading at top), separated by 10 minute intertrial intervals. Timing with respect to infusion start is denoted at top. **(b)** Time courses of MRI signal change observed in ROIs defined around the

cell pellet. Labeled traces denote CTZ injection trials 1, 2, and 3, and the infusion periods are denoted by blue shading. **(c)** Maps of mean response amplitude (5 min following CTZ start) and recovery amplitude (8 min after CTZ infusion end) averaged over the three CTZ infusion trials in an ROI around the luminescent xenograft.



**Extended Data Fig. 8 | Raw time series data following intravenous CTZ delivery.** Individual image frames from an experiment as in Fig. 4a, showing raw MRI scans (top) and signal changes from baseline (bottom) at time points ( $t$ ) relative to the signal peak time (red bar), denoted in minutes below each frame.

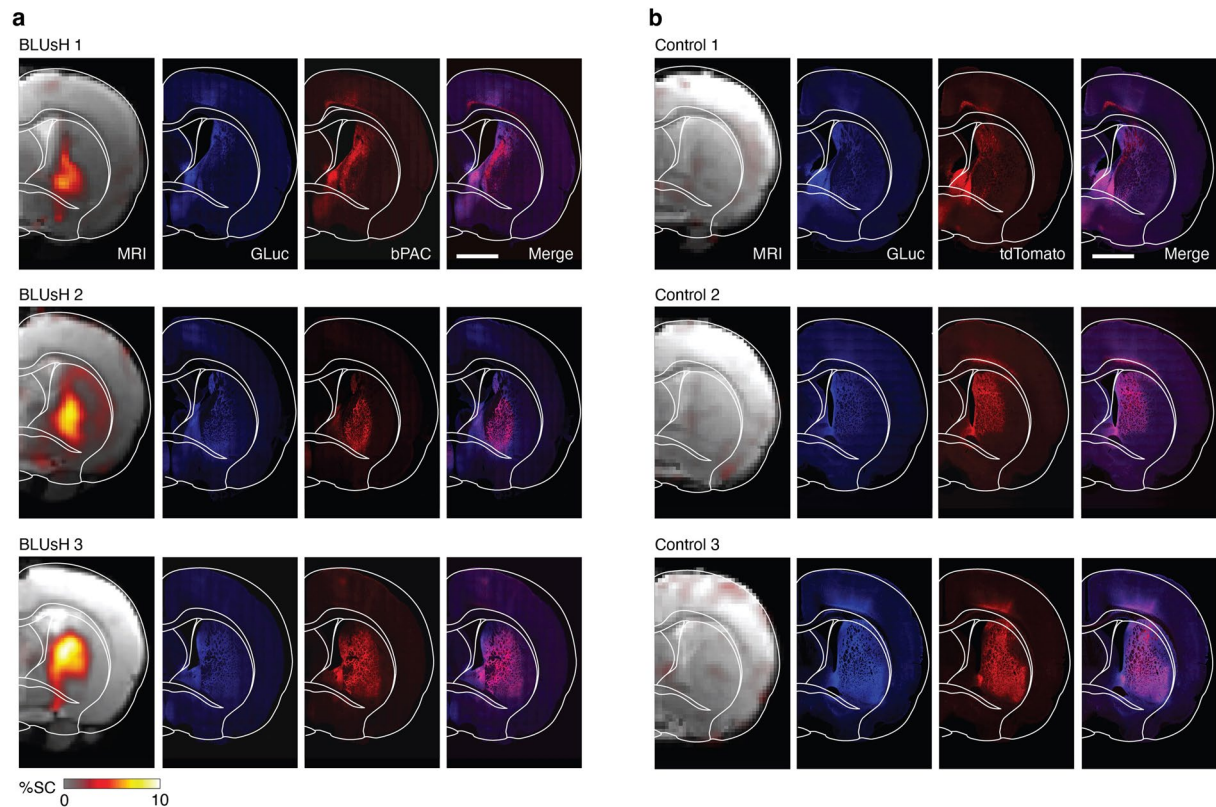
Grey scales denote arbitrary intensity units (AU, top) or percent signal change (%SC, bottom). The location and timing of the peak BLUsH response in this experiment is indicated by the yellow arrowhead.



**Extended Data Fig. 9 | BLUsH and control imaging of virally driven luciferase expression. (a)** Imaging data from five rats that underwent BLUsH imaging of AAV-driven GLucM23 expression following intravenous CTZ delivery in the experiments of Fig. 4. Data are shown over six coronal slices with bregma

coordinates noted in yellow at top. **(b)** Corresponding MRI data obtained from three control virus-treated animals that also express GLucM23 following AAV infection.





**Extended Data Fig. 10 | Extended histology data from BLUsH and control experiments.** (a) Data corresponding to Fig. 4d, showing BLUsH MRI maps (left), GLucM23 staining (blue), bPAC staining (red), and merged images for three individual rats examined by postmortem histology. (b) Analogous MRI and histology data from three animals that received control viruses in place of BLUsH

components. The control treatment results in vascular tdTomato expression (red) in place of bPAC. AAV-directed GLucM23 delivery is identical between BLUsH and control animals and results in robust expression (blue) without corresponding MRI signal changes (left).

## Reporting Summary

Nature Portfolio wishes to improve the reproducibility of the work that we publish. This form provides structure for consistency and transparency in reporting. For further information on Nature Portfolio policies, see our [Editorial Policies](#) and the [Editorial Policy Checklist](#).

### Statistics

For all statistical analyses, confirm that the following items are present in the figure legend, table legend, main text, or Methods section.

n/a Confirmed

- |                                     |                                     |  |
|-------------------------------------|-------------------------------------|--|
| <input type="checkbox"/>            | <input checked="" type="checkbox"/> | The exact sample size ( $n$ ) for each experimental group/condition, given as a discrete number and unit of measurement  |
| <input type="checkbox"/>            | <input checked="" type="checkbox"/> | A statement on whether measurements were taken from distinct samples or whether the same sample was measured repeatedly  |
| <input type="checkbox"/>            | <input checked="" type="checkbox"/> | The statistical test(s) used AND whether they are one- or two-sided<br><i>Only common tests should be described solely by name; describe more complex techniques in the Methods section.</i>   |
| <input checked="" type="checkbox"/> | <input type="checkbox"/>            | A description of all covariates tested   |
| <input type="checkbox"/>            | <input checked="" type="checkbox"/> | A description of any assumptions or corrections, such as tests of normality and adjustment for multiple comparisons  |
| <input type="checkbox"/>            | <input checked="" type="checkbox"/> | A full description of the statistical parameters including central tendency (e.g. means) or other basic estimates (e.g. regression coefficient) AND variation (e.g. standard deviation) or associated estimates of uncertainty (e.g. confidence intervals) |
| <input type="checkbox"/>            | <input checked="" type="checkbox"/> | For null hypothesis testing, the test statistic (e.g. $F$ , $t$ , $r$ ) with confidence intervals, effect sizes, degrees of freedom and $P$ value noted<br><i>Give <math>P</math> values as exact values whenever suitable.</i>                            |
| <input checked="" type="checkbox"/> | <input type="checkbox"/>            | For Bayesian analysis, information on the choice of priors and Markov chain Monte Carlo settings   |
| <input checked="" type="checkbox"/> | <input type="checkbox"/>            | For hierarchical and complex designs, identification of the appropriate level for tests and full reporting of outcomes   |
| <input type="checkbox"/>            | <input checked="" type="checkbox"/> | Estimates of effect sizes (e.g. Cohen's $d$ , Pearson's $r$ ), indicating how they were calculated   |

Our web collection on [statistics for biologists](#) contains articles on many of the points above.

### Software and code

Policy information about [availability of computer code](#)

Data collection Paravision 6.1 (Bruker), Zeiss Zen 3.4, SoftMax Pro (MDC).

Data analysis MATLAB 2021a (Mathworks), AFNI (NIH), GraphPad Prism 9 and 10, ImageJ 2.9.0 (NIH).

For manuscripts utilizing custom algorithms or software that are central to the research but not yet described in published literature, software must be made available to editors and reviewers. We strongly encourage code deposition in a community repository (e.g. GitHub). See the Nature Portfolio [guidelines for submitting code & software](#) for further information.

### Data

Policy information about [availability of data](#)

All manuscripts must include a [data availability statement](#). This statement should provide the following information, where applicable:

- Accession codes, unique identifiers, or web links for publicly available datasets
- A description of any restrictions on data availability
- For clinical datasets or third party data, please ensure that the statement adheres to our [policy](#)

The main data supporting the results in this study are available within the paper and its Supplementary Information. The MRI atlas used for this study was downloaded from <https://www.nitrc.org/projects/whs-sd-atlas>. Source data are provided with this paper. The raw and analysed datasets generated during the study are available for research purposes from the corresponding author on reasonable request.

## Research involving human participants, their data, or biological material

Policy information about studies with [human participants or human data](#). See also policy information about [sex, gender \(identity/presentation\), and sexual orientation](#) and [race, ethnicity and racism](#).

Reporting on sex and gender

Reporting on race, ethnicity, or other socially relevant groupings

Population characteristics

Recruitment

Ethics oversight

Note that full information on the approval of the study protocol must also be provided in the manuscript.

## Field-specific reporting

Please select the one below that is the best fit for your research. If you are not sure, read the appropriate sections before making your selection.

☒ Life sciences ☐ Behavioural & social sciences ☐ Ecological, evolutionary & environmental sciences

For a reference copy of the document with all sections, see [nature.com/documents/nr-reporting-summary-flat.pdf](https://www.nature.com/documents/nr-reporting-summary-flat.pdf)

## Life sciences study design

All studies must disclose on these points even when the disclosure is negative.

Sample size

Data exclusions

Replication

Randomization

Blinding

## Reporting for specific materials, systems and methods

We require information from authors about some types of materials, experimental systems and methods used in many studies. Here, indicate whether each material, system or method listed is relevant to your study. If you are not sure if a list item applies to your research, read the appropriate section before selecting a response.

### Materials & experimental systems

n/a	Included in the study
<input type="checkbox"/>	<input checked="" type="checkbox"/> Antibodies
<input type="checkbox"/>	<input checked="" type="checkbox"/> Eukaryotic cell lines
<input checked="" type="checkbox"/>	<input type="checkbox"/> Palaeontology and archaeology
<input type="checkbox"/>	<input checked="" type="checkbox"/> Animals and other organisms
<input checked="" type="checkbox"/>	<input type="checkbox"/> Clinical data
<input checked="" type="checkbox"/>	<input type="checkbox"/> Dual use research of concern
<input checked="" type="checkbox"/>	<input type="checkbox"/> Plants

### Methods

n/a	Included in the study
<input checked="" type="checkbox"/>	<input type="checkbox"/> ChIP-seq
<input checked="" type="checkbox"/>	<input type="checkbox"/> Flow cytometry
<input type="checkbox"/>	<input checked="" type="checkbox"/> MRI-based neuroimaging

## Antibodies

Antibodies used

Primary: Anti-mCherry (1:250 dilution, LS-C204207, Lifespan Biosciences, Seattle, WA), Anti-tdTomato (1:250 dilution, LS-C340696, Lifespan Biosciences, Seattle, WA) and Anti-HA (1:250 dilution, NB600-363, Novus Biologicals, Centennial, CO), Anti-His (1:250 dilution, MA5-33032, Invitrogen, Waltham, MA), Anti-mCherry (1:500 dilution, ab205402, Abcam, Cambridge, UK), Anti-HA (1:500

dilution, ab9110, Abcam, Cambridge, UK), Anti-Iba1 (1:500 dilution, ab5076, Abcam, Cambridge, UK), Anti-nitrotyrosine (MilliporeSigma AB5411, 1:200).

Secondary: Anti-Goat Alexa Fluor 594 (1:500 dilution, ab150132, Abcam, Cambridge, UK), Anti-Rabbit Alexa Fluor 405 (1:500 dilution, ab175651, Abcam, Cambridge, UK), Anti-Chicken Alexa Fluor 647 (1:500 dilution, A78952, Invitrogen, Waltham, MA), Anti-Rabbit Rhodamine Red (1:200 dilution, 711-295-152, Jackson ImmunoResearch, West Grove, PA), Anti-Goat Alexa Fluor 488 (1:500 dilution, 705-545-003, Jackson ImmunoResearch, West Grove, PA).

#### Validation

Only commercial antibodies from respected sources were used.

Anti-mCherry: Validated for IF, IHC and WB by LSBio. Applied in murine IHC in <https://doi.org/10.1016/j.neuron.2016.04.017>

Anti-tdTomato: Validated for IHC/IF/WB by LSBio. Applied for murine IHC in multiple publications e.g. DOI: 10.1002/cne.25061

Anti-HA: validated for IP/ICC/IF by Abcam, validated for murine IHC by multiple publications e.g. <https://doi.org/10.1038/s41467-019-09298-4>

Anti-His: validated for WB/IHC/ICC/IF/IP by Invitrogen

Anti-mCherry (Abcam): validated for WB and ICC/IF by Abcam, validated for murine IHC by multiple publications e.g. doi: 10.4103/1673-5374.295925

Anti-iba1: validated for IHC/WB by Abcam. Applied for murine IHC in multiple publications e.g. <https://doi.org/10.1016/j.celrep.2018.08.001>

Anti-nitrotyrosine: validated for IHC by Chemicon

## Eukaryotic cell lines

Policy information about [cell lines and Sex and Gender in Research](#)

#### Cell line source(s)

CHO K1 and A7r5 cells (MilliporeSigma), HEK 293 FreeStyle and 293FT cells (Thermo Fisher)

#### Authentication

Commercially available cell lines were validated by the manufacturer by morphology STR analysis and DNA barcoding, and morphology was confirmed by us before use.

#### Mycoplasma contamination

The cell lines tested negative for mycoplasma contamination in the MycoAlert assay (Lonza, Walkersville, MD, USA).

#### Commonly misidentified lines (See [ICLAC](#) register)

No commonly misidentified cell lines were used.

## Animals and other research organisms

Policy information about [studies involving animals; ARRIVE guidelines](#) recommended for reporting animal research, and [Sex and Gender in Research](#)

#### Laboratory animals

Male Sprague-Dawley rats (200–250 g, 7–8-weeks old)

#### Wild animals

The study did not involve wild animals.

#### Reporting on sex

The study was performed on male animals only.

#### Field-collected samples

The study did not involve samples collected from the field.

#### Ethics oversight

All procedures were performed in strict compliance with US Federal guidelines, with oversight by the MIT Committee on Animal Care.

Note that full information on the approval of the study protocol must also be provided in the manuscript.

## Magnetic resonance imaging

### Experimental design

#### Design type

Drug response or single-stimulus response.

#### Design specifications

Animals were imaged before, during and after the administration of luciferase substrates or of stimulation with single blocks of illumination under the conditions noted in the text.

#### Behavioral performance measures

This study was performed in anesthetized animals and did not involve behavioural performances.

### Acquisition

#### Imaging type(s)

Functional and structural.

#### Field strength

9.4T

#### Sequence & imaging parameters

Anatomical MRI images were acquired using a longitudinal relaxation time (T2)-weighted rapid acquisition with refocused echoes (RARE) pulse sequence with RARE factor = 8, bandwidth = 200 kHz, effective echo time (TE) = 30 ms, repetition time (TR) = 5 s, in-plane field of view (FOV) = 2.56 × 2.56 cm<sup>2</sup>, in-plane resolution of 100 × 100 μm<sup>2</sup> and slice thickness = 1 mm. Functional scan series were acquired using a standard gradient echo echo-planar imaging (EPI) pulse



sequence with TE values = 20 ms; flip angle = 90°, TR = 2 s, FOV = 2.56 × 2.56 cm<sup>2</sup> and in-plane resolution of 400 × 400 μm<sup>2</sup> with slice thickness = 1 mm.

Area of acquisition

Slices at or adjacent to injection or viral treatment sites, as noted in the text.

Diffusion MRI

☐

Used

☒

Not used

## Preprocessing

Preprocessing software

Paravision 6.1 (reconstruction) and AFNI (slice timing correction, motion correction, intensity normalization, smoothing, resampling)

Normalization

Data were registered to a Waxholm space rat brain atlas.

Normalization template

Papp, E.A., Leergaard, T.B., Calabrese, E., Johnson, G.A. & Bjaalie, J.G. Waxholm Space atlas of the Sprague Dawley rat brain. Neuroimage 97, 374-386 (2014)

Noise and artifact removal

Gaussian smoothing with a spatial kernel of 0.5 mm FWHM was applied during preprocessing.

Volume censoring

Not done

## Statistical modeling & inference

Model type and settings

Comparisons of mean fMRI amplitudes were performed using Student's t-test. Correlation coefficients were evaluated using Fisher's Z-test.

Effect(s) tested

Responses to photostimulation and CTZ injection.

Specify type of analysis:

☐

Whole brain

☐

ROI-based

☒

Both

Anatomical location(s)

Regions of interest were defined with respect to fiber coordinates, cannula coordinates, or response maxima.

Statistic type for inference

ROI-wise

(See [Eklund et al. 2016](#))

Correction

Statistical thresholds noted throughout.

## Models & analysis

n/a | Involved in the study

☒

Functional and/or effective connectivity

☒

Graph analysis

☒

Multivariate modeling or predictive analysis